Mass-Imbalanced Hubbard Model on a 2D Square Lattice

by

© *Amir Kaffashnia*

A thesis submitted to the School of Graduate Studies

in partial fulfilment of the requirements for the degree of

Master of *Science*

Department of Physics and Physical Oceanography

Memorial University of Newfoundland

July 2019

St. John's Newfoundland

Abstract

The Hubbard model (HM) and the Falicov-Kimball model (FKM), which are two standard models of strongly correlated electrons, provide an interesting benchmark for the physics of locally correlated systems. We study the intermediate model, mass-imbalanced Hubbard model at half-filling on a 2D square lattice which connects continuously the HM to the FKM. We employ dynamical mean field theory (DMFT) and dynamical cluster approximation (DCA) using continuous-time auxiliary field method (CT-AUX) as self-consistent impurity solver to study the single particle spectral function and self-energy allowing us to map-out the phase diagram of the system. Solutions to the mass-imbalanced model cannot enforce paramagnetic self-consistency and therefore at low temperature result in paramagnetic (PM) to antiferromagnetic (AFM) transition. In addition, in the PM state and at finite temperature, we observed a spin dependent crossover from Fermi liquid (FL) regime to non-Fermi liquid (nFL) regime in which the FL regime is destroyed, monotonically, induced not only by the interaction but also by the mass imbalance. We present the results for small cluster DCA and explore its dependency on cluster size as well.

Acknowledgements

I want to express my gratitude to Dr. James LeBlanc for supervising this master thesis and appreciate his patience and tremendous help. His office door was always open whenever I ran into a trouble spot or had a question about my research or writing. I have greatly benefited from the critical discussions with Amir Taheridehkordi about the physics of many-body systems and numerical methods. I would also like to thank the examiners who were involved in the validation survey for this research project: Dr. Mykhaylo Evstigneev and Dr. Stefan Wallin.

I gratefully acknowledge the Department of Physics and Physical Oceanography and financial support by the School of Graduate Studies at Memorial University of Newfoundland.

I would like to thank my loving, supportive, encouraging and patient wife Arzu Safarlou who inspired me to pursue my dreams. Her faithful support during my study is so appreciated.

Finally, I am grateful for my parents love and support. Without the inspiration, drive, and support that they have given me, I might not be the person I am today.

Contents

List of Tables

List of Figures

List of Abbreviations and Symbols

HM	Hubbard Model
FKM	Falicov-Kimball Model
DMFT	Dynamical Mean Field Theory
DCA	Dynamical Cluster Approximation
CT-QMC	Continuous Time Quantum Monte Carlo
CT-AUX	Continuous Time Auxiliary field method
AIM	Anderson Impurity Model
2D	2 Dimensional
MI	Metal-Insulator
AFM	Antiferromagnetic
PM	Paramagnetic
FL	Fermi liguid
nFL	non-Fermi liguid
MAXENT	Maximum Entropy Method
FS	Fermi Surface
$Im\Sigma$	Imaginary part of the self energy
ImG	Imaginary part of the Green's function
Z	Quasiparticle renormalization

$i\omega$	Matsubara frequency
t_f	Mass imbalance parameter
U	Hubbard interaction
μ	Chemical potential
β	Inverse temperature
T	Temperature
m^*	Effective mass
m	Electron's bare mass

Chapter 1

Introduction

1.1 Strongly Correlated Systems

All natural sciences including physics have to find methods to determine the characteristics of the systems they study. Generally speaking, they are putting the system in interaction with some external probe and measure the response of the system. If the particles constituting the system weakly interact with this external probe or with each other, the response of the system will be a linear function of the interaction strength. From this point of view, this situation is one electron picture in solid state physics that has many useful results [1].

However, there are very important systems for which interactions between constituent particles with the external probe or with each other are strong. These strong interactions play a key role in determining the properties of these systems. Conventional superconductors, high-temperature superconductors, magnetic systems, quantum Hall systems, one-dimensional electron systems and the insulating state of bosonic atoms in a periodic potential are very well known examples for strongly correlated systems.

A theoretical model is necessary to provide a deeper understanding of various properties of these kind of systems. One really good model is the Hubbard model (HM), which was originally proposed in 1963, independently by Martin Gutzwiller [2], Junjiro Kanamori [3] and, of course, John Hubbard [4] to describe electrons in solids. Originally, the model was introduced to explain the metal-insulator (MI) transition which was one of the interesting topics around the middle of last century. After publishing his model in 1963, Hubbard continued to improve it and in the next year he introduced his Hubbard-III approximation which became especially important in the MI transition area [5]. In 1969, Mott used Hubbard-III approximation and the properties of particle correlations in introducing his very well known Mott (Mott-Hubbard) MI transition [6]. Mott transition is a type of MI transition even for an odd number of electrons per site (i.e. MI transition in the half filling). This interesting feature could not be understood in terms of conventional band theory stating that a half-filled band always leads to a conducting state.

1.2 Tight Binding and Hubbard Models

Tight binding has been used for many years as a convenient and transparent model for describing the electronic structure in solids wherein electrons can hop between lattice sites without feeling each other. In this model, the hopping can only happen between nearest-neighbour sites, and all hopping processes have the same kinetic energy, $-t$. The tight-binding model has played a key role in the emergence of an electronic band structure which also was important in the development of the semiconductor technology [7].

The Hubbard model is an extension of the tight-binding model in which the Hamiltonian features an additional term representing an effective Coulomb repulsion U. This

energy amount which is for each pair of electrons occupying the same lattice site, is also called on site or local interaction. In HM like tight binding model, the wave function of an electron is centered on the lattice site of an ion and any electron can hop one lattice spacing at a time (Fig. 1.1). Therefore, the Hamiltonian of the HM consists of the kinetic term H_0

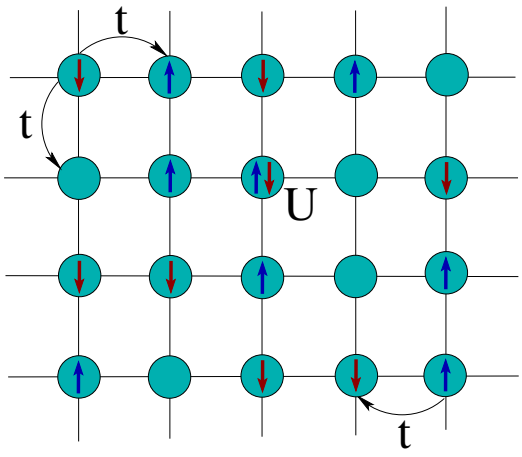

Figure 1.1 – A schematic figure of the Hubbard model on a 2D square lattice, where t is the hopping term and U is the onsite repulsive energy. The green circles represent the lattice sites of ions where the spin-up and spin-down electrons are centered on.

and interaction term H_I [1]:

$$H = H_0 + H_I \tag{1.1}$$

where,

$$H_0 = \sum_{i,j} \sum_{\mu,\nu} T_{i,j}^{\mu,\nu} \hat{c}_{i,\mu}^{\dagger} \hat{c}_{j,\nu} \tag{1.2}$$

In Eq. (1.2), $T_{i,j}^{\mu,\nu}$ is the hopping amplitude and is :

$$T_{i,j}^{\mu,\nu} = \int d^3x \phi_{\mu}^*(x - R_i)\phi_{\nu}(x - R_j) \times [-\frac{\hbar^2}{2m}\nabla^2 + V(x)] \tag{1.3}$$

where $V(x)$ is the crystal ion potential felt by a single electron and ϕ_μ and ϕ_ν are atomic orbitals in an atom at lattice sites i and j respectively. The interaction term in Eq. (1.1) is:

$$H_I = \frac{1}{2} \sum_{i,j,k,l} \sum_{\mu,\nu,\sigma\tau} \langle i,\mu,j,\nu| \frac{1}{r} |k,\sigma,l,\tau\rangle \, \hat{c}^\dagger_{i,\mu} \hat{c}^\dagger_{j,\nu} \hat{c}_{k,\sigma} \hat{c}_{l,\tau} \tag{1.4}$$

where $\langle i,\mu,j,\nu| \frac{1}{r} |k,\sigma,l,\tau\rangle$ is matrix elements of the Coulomb interaction between electrons on different lattice sites. Hubbard simplified Eq. (1.4) and since the interaction between electrons in orbitals on the same site (ions) is the most important one, he only considered the matrix elements in which $i = j = k = l$ and supposed the existence of only one orbital. Therefore, after these assumptions and simplifications, Eq. (1.4) takes the form:

$$H_I = U \sum_i n_{i,\uparrow} n_{i,\downarrow} \tag{1.5}$$

where

$$U = \langle ii| \frac{1}{r} |ii\rangle \tag{1.6}$$

represents the Coulomb repulsion on the same site. The kinetic term is [1]:

$$T^{\mu,\nu}_{i,j} = T_0 \delta^{\mu\nu} \delta_{ij} + t^{\mu\nu}_{ij} \tag{1.7}$$

Considering only the nearest neighbor hopping, the first term in Eq. (1.7) is zero and the second term is non zero. So, the Hamiltonian of a one-band Hubbard model takes the following form:

$$H = -t \sum_{\langle ij\rangle,\sigma} (\hat{c}^\dagger_{i\sigma} \hat{c}_{j\sigma} + \hat{c}^\dagger_{j\sigma} \hat{c}_{i\sigma}) + U \sum_i \hat{n}_{i\uparrow} \hat{n}_{i\downarrow} \tag{1.8}$$

where $\hat{c}^\dagger_{i\sigma}$ and $\hat{c}_{i\sigma}$ create and annihilate, respectively, one of the two electrons with spin σ, while $\hat{n}_{i\sigma} = \hat{c}^\dagger_{i\sigma} \hat{c}_{i\sigma}$ is the occupancy operator at the site i. $U > 0$ denotes the on-site repul-

sive interaction of different species and $\langle ij \rangle$ denotes two nearest-neighbor sites belonging to different sublattices [1, 4].

In spite of its simple form, Hubbard Hamiltonian has so far only been exactly solved for the one-dimensional case in which the Hamiltonian is [8]:

$$H = -t \sum_{i,\sigma} (\hat{c}^{\dagger}_{i+1\sigma} \hat{c}_{i\sigma} + \hat{c}^{\dagger}_{i\sigma} \hat{c}_{i+1\sigma}) + U \sum_{i} \hat{n}_{i\uparrow} \hat{n}_{i\downarrow} \tag{1.9}$$

It worth mentioning that the results obtained for one-dimensional systems are very susceptible to the details of the problem. For instance, considering hopping between only nearest neighbours and adding the next nearest neighbours give rise to unmagnetized and ferromagnetic properties respectively [9, 10].

Therefore, the Hubbard Hamiltonian is only apparently simple, because when it is written down, not only it is a hard problem mathematically but also its physics is too complicated and very sensitive to the details. However, nowadays thanks to computer power, numerical simulations of the model are achievable. Let us mention here that the known numerical methods are approximate solutions, however, for the 2D Hubbard model numerical methods have been shown to converge to the same results [11].

1.3 Falicov-Kimball Model

While the Hubbard-III was the first satisfactory modeling of Mott transition with one electron per lattice site, it already reveals the principal components of the Falicov-Kimball model (FKM) [12]. FKM is a simple model that was originally proposed for a semiconductor to metal transition, based on the existence of both localized and itinerant interacting quasiparticle states. In this model, there are two species of electrons with different effec-

tive masses: one species has infinite mass so the electrons do not move, while the second species represents itinerant electrons which have hopping term as their kinetic energy.

FKM can be seen as a simplification of the Hubbard model achieved by neglecting the kinetic (hopping) energy of the spin-up or spin-down particles which are infinitely massive [13]. In another interpretation, FKM is a model for crystallization in which heavy particles are considered as ions [14]. These two species of electrons are coupled through an on-site interaction U. The Hamiltonian of the model is:

$$H = -\sum_{i,j\in\Lambda} t_{ij}\hat{c}_i^\dagger \hat{c}_j + U\sum_{i\in\Lambda} W(i)\hat{n}_i \tag{1.10}$$

where $\Lambda \subset \mathbb{Z}$ is usually taken to be a square lattice and $t_{ij} = 1$ if i and j are nearest neighbour and zero otherwise. In Eq. (1.10) $\hat{c}_i^\dagger, \hat{c}_i$ denote creation, annihilation operators of an electron at site i, $\hat{n}_i = \hat{c}_i^\dagger \hat{c}_i$ and $W(i) = 0, 1$ is the number of localized or heavy electrons at site i [14].

1.4 Fermi Liquid and Non-Fermi Liquid States

While the Fermi liquid (FL) state shows strong metallic behavior, the non-Fermi liquid (nFL) are classified as unconventional metals[1]. Since they have shown strong quantum fluctuations near Fermi surfaces, their physical properties qualitatively deviate from those of non-interacting fermions. Due to a lack of theoretical methods and in the absence of well-defined quasiparticles, it has been difficult to understand the universal physics of nFL; however, the universal physics of nFL is captured by interacting field theories which replace Landau Fermi liquid theory [16].

[1]The nFL state is called bad metallic state in the literature [15].

A fundamental difference between the FKM and the HM is that while the metallic state in the HM was described by a Fermi liquid (FL), the metallic state in the FKM is a non-Fermi liquid (nFL) with no quasiparticles. In the FKM limit due to the random distributions of the immobile electrons on the lattice, the translational symmetry is broken, which leads to this exotic state [17, 18].

1.5 Objective

HM and FKM have a long history. These two models together are the most studied models to describe correlation effects in interacting fermion systems. However, the region between these two limits is still unknown for different lattices. We believe that, the evolution between these two situations is far from trivial; consequently, we tune our model continuously from the FKM to the HM allowing us to study this intermediate model which is called mass-imbalanced Hubbard model [2]. We investigate this region by increasing the hopping amplitude of the localized heavy electrons from zero to the same amplitude as itinerant light electrons. Here, the term mass imbalance refers to different hopping amplitudes for spin-up and spin-down electrons.

The mass-imbalanced HM in the solid state is difficult to realize; however, with the emerging of cold atom systems such mass imbalances in a two-component system can be realized readily. This realization which can be done either by different atomic species [21] or by having a spin-dependent hopping [22], have been the subjects of intensive research [19, 20, 23–29]. Phase diagram of the ground state of the mass-imbalanced HM in the context of two component fermionic mixture in 3D optical lattice has been studied before

[2] In the literature, it is also called asymmetric Hubbard model [17, 19, 20].

by dynamical mean field theory (DMFT) [15, 17, 30, 31]. Magnetic phase diagram of such a two species of repulsively interacting fermionic cold atom in optical latices (cubic lattice) has been investigated by DMFT; and, the same magnetic phase behaviour has been expected for a 2D system with square lattice geometry, which is the topic of the present thesis [32]. We are interested to investigate the magnetic phase diagram of the mass-imbalanced HM on a 2D square lattice using DMFT.

Since the metallic state in the HM is a Fermi liquid and in the FKM, it is a non-Fermi liquid with no quasiparticles, we are interested to study the metallic state in the mass imbalanced HM and we expect that in our system the Fermi liquid to non-Fermi liquid crossover can occur. We also would like to study the spectral function in real frequency, double occupancy and mass renormalization which help us to have a better understanding of the model.

In chapter 2 we introduce the model and the method employed: DMFT and dynamical cluster approximation (DCA) using continuous time auxiliary field (CT-AUX) simulations as an impurity solver. In chapter 3 we present the calculated phase diagram of the mass-imbalanced HM, the self-energy, Green's function, spectral function, double occupancy, and mass renormalization. Finally, in chapter 4 we summarize our results and discuss the underlying physics of the phase transition and the results for physical quantities.

Chapter 2

Model and Methods of Calculation

2.1 Model

In the mass-imbalanced Hubbard model, the spin symmetry ($SU(2)$ symmetry) and the time-reversal symmetry are both broken, nonetheless, this system can be readily implemented in an optical lattice by loading a mixture of two ultracold fermionic atomic species with different masses [23]. In general, as mentioned in section (1.5), mass-imbalance can be obtained either by having two different species with two different orbitals or by generating spin-dependent hopping within one orbital. In the present work, we adopt the notation of two spin projections $\uparrow$ and $\downarrow$; hence, the Hamiltonian of the mass-imbalanced HM for one orbital takes the following form:

$$H = -\sum_{\sigma\in\{\uparrow,\downarrow\}} t_\sigma \sum_{\langle ij\rangle} (\hat{c}^\dagger_{i\sigma}\hat{c}_{j\sigma} + \hat{c}^\dagger_{j\sigma}\hat{c}_{i\sigma}) + U\sum_i \hat{n}_{i\uparrow}\hat{n}_{i\downarrow} \tag{2.1}$$

where $t_{\uparrow(\downarrow)}$ is the hopping amplitude of the spin-up (-down) particles and indicates the main deference between the Hamiltonian of the HM and the mass-imbalanced one. While hopping amplitude in the Hamiltonian of the HM was independent of the σ (Eq. 1.8), in

the mass-imbalanced HM it depends on σ. Thus, in the mass-imbalanced case the hopping amplitude is different for the spin-up and spin-down $t_\uparrow \neq t_\downarrow$. In Eq. (2.1), $U > 0$ is the on-site repulsive interaction between the two spin species [1]. Let us mention here again that in the Hamiltonian (2.1), the chemical potential is $\mu = 0$ which means we restrict ourselves to the interesting case of half filling such that the total number of electrons per site $n_\uparrow + n_\downarrow = 1$. So, this Hamiltonian corresponds to the single-band approximation. If we rewrite the Hamiltonian (2.1), we will have:

$$H = -t_\uparrow \sum_{\langle ij \rangle} (\hat{c}^\dagger_{i\uparrow} \hat{c}_{j\uparrow} + \hat{c}^\dagger_{j\uparrow} \hat{c}_{i\uparrow}) - t_\downarrow \sum_{\langle ij \rangle} (\hat{c}^\dagger_{i\downarrow} \hat{c}_{j\downarrow} + \hat{c}^\dagger_{j\downarrow} \hat{c}_{i\downarrow}) + U \sum_i \hat{n}_{i\uparrow} \hat{n}_{i\downarrow} \tag{2.2}$$

We suppose the hopping parameters $t_\uparrow$ and $t_\downarrow$ refer to light $\uparrow$ and heavy $\downarrow$ electrons, respectively, so that $t_\uparrow \geqslant t_\downarrow \geqslant 0$. By dividing both sides of Eq. (2.2) by $t_\uparrow$, the mass-imbalanced Hamiltonian takes the following form:

$$\frac{H}{t_\uparrow} = -\sum_{\langle ij \rangle} (\hat{c}^\dagger_{i\uparrow} \hat{c}_{j\uparrow} + \hat{c}^\dagger_{j\uparrow} \hat{c}_{i\uparrow}) - \frac{t_\downarrow}{t_\uparrow} \sum_{\langle ij \rangle} (\hat{c}^\dagger_{i\downarrow} \hat{c}_{j\downarrow} + \hat{c}^\dagger_{j\downarrow} \hat{c}_{i\downarrow}) + \frac{U}{t_\uparrow} \sum_i \hat{n}_{i\uparrow} \hat{n}_{i\downarrow} \tag{2.3}$$

Henceforth, we set $t_\uparrow \equiv 1$ as our unit of energy and do the calculations for different values of the mass imbalance parameter[2] which we define as $t_f \equiv \frac{t_\downarrow}{t_\uparrow}$, a quantity which goes from 1 (mass-balanced HM) to 0 (Falicov-Kimball limit with the maximum mass-imbalance). Therefore, in the half filling and FKM case when the down spins become infinitely heavy, the model is now a field of light up spins, moving on a static background of down spins which are stationary. Similarly, as $t_f \to 1$ the down spins move just as well and we recover the standard Hubbard model. Thus, by decreasing the t_f, indeed we increase the mass-imbalance.

[1] Physics of $U < 0$ case at half filling, is related by a particle hole transformation [23].

[2] There is a different convention to define the mass-imbalance parameter. For instance, [30] defines the mass-imbalance as $z \equiv \frac{t_\uparrow - t_\downarrow}{t_\downarrow + t_\downarrow}$

Note that the Hamiltonian (2.1), in the strong-coupling limit $U \gg t_\uparrow, t_\downarrow$ and near half filling, can be mapped onto an effective spin Hamiltonian [3] [32–34]:

$$H_{eff} = J_\parallel \sum_{\langle ij \rangle} \hat{S}_i^z \hat{S}_j^z + J_\perp \sum_{\langle ij \rangle} (\hat{S}_i^x \hat{S}_j^x + \hat{S}_i^y \hat{S}_j^y) \tag{2.4}$$

where longitudinal coupling constant $J_\parallel$ is:

$$J_\parallel = \frac{2(t_\uparrow^2 + t_\downarrow^2)}{U} \tag{2.5}$$

transverse coupling constant $J_\perp$:

$$J_\perp = \frac{4 t_\uparrow t_\downarrow}{U} \tag{2.6}$$

and the spin-1/2 operator [23]:

$$\hat{S}_i^\alpha = \frac{1}{2} \sum_{\mu\nu} \hat{c}_{i\mu}^\dagger \sigma_{\mu\nu}^\alpha \hat{c}_{i\nu} \tag{2.7}$$

where σ^α are the Pauli matrices. In the presence of mass-imbalance, i.e., $t_\uparrow \neq t_\downarrow$, the longitudinal coupling (antiferromagnetic coupling in Z direction) is always greater than the transverse coupling ($J_\parallel \geqslant J_\perp$) and the Hamiltonian (2.4) is the anisotropic Heisenberg model. In the limit of large hopping imbalance ($t_\uparrow \gg t_\downarrow$), $J_\parallel \gg J_\perp$; therefore, the second term in the Hamiltonian (2.4) is considered as a perturbation, and we arrive at the Ising model [32]. Note that mapping the Hamiltonian (2.1) to the effective spin Hamiltonian (2.4) is presented in order to have a better physical understanding of the mass-imbalanced system. Naturally, for quantitative theoretical predictions, particularly, in the intermediate coupling region ($t_\alpha \sim U$), it is necessary to use non-perturbative numerical methods.

[3] or spin-1/2 XXZ model [23].

2.2 Background Information and Methods

We first introduce some parameters and notation that will be used frequently in our results section. We start to give a brief review of imaginary time Green's functions and self-energy. We then also review important aspects of the mass renormalization. There are numerous excellent textbooks relevant to condensed matter physics where more details can be found [35]. After reviewing the background materials, we will discuss the methods employed.

2.2.1 Green's Function and Self-Energy

The thermal average of any operator $\hat{O}$ is:

$$\langle \hat{O} \rangle_{th} = \frac{1}{\mathcal{Z}} Tr\Big(e^{-\beta(H-\mu N)} \hat{O} \Big) \tag{2.8}$$

where β and μ are the inverse temperature and chemichal potential, respectively. $\mathcal{Z}$ is the grand partition function and is equal to:

$$\mathcal{Z} = Tr\Big(e^{-\beta(H-\mu N)} \Big) \tag{2.9}$$

By introducing the imaginary-time Heisenberg operator:

$$c_\alpha(\tau) = e^{\tau K} c_\alpha e^{-\tau K} \tag{2.10}$$

in which $K = H - \mu N$, the imaginary time Green function would be:

$$\begin{aligned} G_{\alpha,\beta}(\tau) &= -\langle T c_\alpha(\tau) c_\beta^\dagger \rangle_{th} = -\theta(\tau) \langle c_\alpha(\tau) c_\beta^\dagger \rangle_{th} + \theta(-\tau) \langle c_\beta^\dagger c_\alpha(\tau) \rangle_{th} \\ &= \frac{1}{\mathcal{Z}} \Bigg(-\theta(\tau) \sum_{ij} e^{-\beta(E_i - \mu N_i)} e^{\tau(E_i - E_j + \mu)} \langle i | c_\alpha | j \rangle \langle j | c_\beta^\dagger | i \rangle \\ &\qquad + \theta(-\tau) \sum_{ij} e^{-\beta(E_i - \mu N_i)} e^{\tau(E_j - E_i + \mu)} \langle i | c_\beta^\dagger | j \rangle \langle j | c_\alpha | i \rangle \Bigg) \end{aligned} \tag{2.11}$$

In Eq. (2.11), α, β denote some set of quantum numbers. $|i\rangle$ are the eigenstates of the system with energies E_i and particle number N_i, and T is imaginary time ordering. From Eq. (2.11) G is well-defined only when $\tau \in [-\beta, \beta]$ and that for $\tau \in [-\beta, 0]$ one has $G(\tau+\beta) = -G(\tau)$. By using the Fourier transform,

$$G(\tau) = \frac{1}{\beta} \sum_{n=-\infty}^{\infty} e^{-i\omega_n \tau} G(i\omega_n) \tag{2.12}$$

or equivalently,

$$G(i\omega_n) = \int_0^{\infty} d\tau e^{i\omega_n \tau} G(\tau) \tag{2.13}$$

the Matsubara Greens function takes the following form,

$$G_{\alpha\beta}(i\omega_n) = \frac{1}{\mathcal{Z}} \sum_{ij} \frac{e^{-\beta(E_i - \mu N_i)} + e^{-\beta(E_j - \mu N_j)}}{i\omega_n + \mu - (E_j - E_i)} \langle i|c_\alpha|j\rangle \langle j|c_\beta^\dagger|i\rangle \tag{2.14}$$

Eq. (2.14) is the Lehmann representation of the Green function. We concentrate on a single band and assume that the z-component of the spin is a good quantum number so that the Green function is a scalar and $\alpha = \beta = (k, \sigma)$. Therefore, the bare Matsubara Green's function would be:

$$G^0(k, i\omega_n) = \frac{1}{i\omega_n - \varepsilon(k) + \mu} \tag{2.15}$$

where μ is chemical potential and $i\omega_n$ are the (Fermionic) Matsubara frequencies and is:

$$i\omega_n = \frac{(2n+1)\pi}{\beta} \tag{2.16}$$

$G(i\omega_n)$ and $G(\tau)$ are related to a real frequency Green's function $G(\omega)$ through,

$$G(i\omega_n) = \frac{-1}{\pi} \int_{-\infty}^{\infty} \frac{d\omega Im[G(\omega)]}{i\omega_n - \omega} \tag{2.17}$$

$$G(\tau_n) = \frac{1}{\pi} \int_{-\infty}^{\infty} \frac{d\omega Im[G(\omega)] e^{-\tau_n \omega}}{1 + e^{-\beta\omega}} \tag{2.18}$$

where the imaginary part of the real frequency Green's function, $Im[G(\omega)]$, in the above equations defines the spectral function in real frequency:

$$A(\omega) = -\frac{1}{\pi} Im[G(\omega)] \tag{2.19}$$

We use the maximum entropy method (MAXENT) [36] to obtain the spectral functions A(ω) in real frequency.

For the interaction case, we have a full Green's function which is the sum over all connected Feynmann diagrams (whereas such an expansion is not possible for the real-time Green function at finite temperature) [35]. The full Green's function is compactly written with Dysons equation as:

$$G(k, i\omega_n) = G^0(k, i\omega_n) + G^0(k, i\omega_n)\Sigma(k, i\omega_n)G(k, i\omega_n) \tag{2.20}$$

Therefore, the self-energy Σ is the sum of all one particle irreducible Feynmann diagrams with two open legs. Dysons equation then generates all diagrams of the interacting Green's function.

2.2.2 Effective Mass

In very general terms, the main effect of the interaction U is to reduce the mobility of the electrons. This phenomenon, which eventually leads to the insulator localization, is measured by the effective (or renormalized) mass of the carriers m^* given by the self-energy Σ. Within DMFT, at low frequencies $\Sigma(i\omega_n) \approx (1 - 1/Z)i\omega_n$ where Z is the quasiparticle weight or renormalization factor. The effective mass $m^* \propto 1/Z$, and for a noninteracting system Z = 1, while the localization is associated to vanishing Z ($Z \to 0$) which is corresponding to an infinite effective mass $m^* \to \infty$. A small value of Z is the signature of a

highly correlated nFL phase. Therefor, within DMFT at low frequencies:

$$m^*/m = Z_\sigma^{-1} = 1 - Im\Sigma_\sigma(i\omega_0)/(i\omega_0) \tag{2.21}$$

where m denotes the electron's bare mass. In the mass-imbalanced HM, because the two species have different bare masses and hoppings, a different renormalization is expected [15, 23, 31].

2.2.3 Dynamical Mean Field Theory (DMFT)

DMFT is one of the most popular modern theoretical approaches to investigate strongly correlated electrons [37]. It has been shown that in the limit of large coordination number the HM can be mapped exactly to the Anderson impurity model (AIM) [38, 39]. DMFT is a time dependent variant of the mean-field theory so that it is able to capture the frequency dependent properties. This method can be applied numerically in the context of real materials, and this has played a key role in the success of the theory. DMFT has provided an important contribution to the understanding and approximate solution of the HM. This point relies on the fact that the DMFT maps the HM to a local AIM. There is a plethora of numerical methods for solving the AIM that can be applied right away to treat the DMFT equations. Examples are the continuous-time Quantum Monte Carlo (CT-QMC) solvers [40, 41], Hirsch-Fye quantum Monte Carlo [42, 43], exact diagonalization [44, 45], and renormalization group approaches [46].

2.2.3.1 Derivation of the DMFT Equations - Effective Anderson Impurity Model

The first derivation of DMFT was done in the limit of infinite dimensions [39]. Nonetheless, infinite dimensions is not the best way to introduce DMFT as an approximation for

a lattice in finite dimensions. A standard derivation of the DMFT in finite dimensions is the cavity construction [37]. In this approach, a representative site is separated from the rest of the lattice which these two parts are coupled to each other via a retarded hybridization function. This local effective medium description, which is equivalent to the AIM, is an exact solution in the limit of large coordination number. Bethe lattice is a very well known example for lattices with a large coordination number. In the cavity method, the representative site (or impurity site) is shown by i (usually by convention set to $i = 0$), and an integral is taking over all other degrees of freedom for the lattice site. At the end, an effective dynamical "Weiss field" in which the lattice site i is embedded is obtained (see Fig. 2.1).

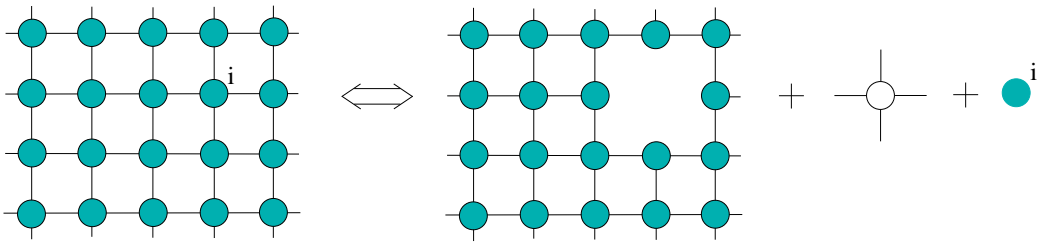

Figure 2.1 – Illustration of the cavity method in the derivation of the DMFT equations. The idea of this method is focusing on a representative site i and separating of the total action S into a sum of the actions arising from the site i, S_0, the hybridization between the site and the lattice ΔS, and the action $S^{(0)}$ lattice without the site i.

For the derivation of the DMFT equations we will formulate the effective action of the HM and then identify it with the action of the AIM to obtain the hybridization and the effective field. For this purpose we are starting with the partition function $\mathcal{Z}$ in the grand

canonical ensemble which is sufficient to describe a thermodynamic system:

$$\mathcal{Z} = \int \prod_i Dc^*_{i\sigma} Dc_{i\sigma} e^{-S} \tag{2.22}$$

where $c^*_{i\sigma}$, $c_{i\sigma}$ are anti commuting Grassmann variables [47], and the action S [48] for the HM is:

$$S = \int_0^\beta d\tau \Bigg(\sum_{i\sigma} c^*_{i\sigma}(\tau) \left[\frac{\partial}{\partial \tau} - \mu \right] c_{i\sigma}(\tau) - \sum_{ij\sigma} t_{ij} c^*_{i\sigma}(\tau) c_{i\sigma}(\tau) + U \sum_i c^*_{i\uparrow}(\tau) c_{i\uparrow}(\tau) c^*_{i\downarrow}(\tau) c_{i\downarrow}(\tau) \Bigg) \tag{2.23}$$

Now, as it was described in Fig. 2.1, we divide the lattice into three parts: the impurity site $i = 0$, the lattice without site $i = 0$, and the part that connects the two. The action correspondingly would be:

$$S = S_0 + \Delta S + S^{(0)} \tag{2.24}$$

where S_0 which is the action only on site $i = 0$ equal to:

$$S_0 = \int_0^\beta d\tau \left(\sum_\sigma c^*_{0\sigma}(\tau) \left[\frac{\partial}{\partial \tau} - \mu \right] c_{0\sigma}(\tau) + U c^*_{0\uparrow}(\tau) c_{0\uparrow}(\tau) c^*_{0\downarrow}(\tau) c_{0\downarrow}(\tau) \right). \tag{2.25}$$

The hybridization between site $i = 0$ and the rest is:

$$\Delta S = -\sum_{i\sigma} t_{i0} c^*_{i\sigma}(\tau) c_{0\sigma}(\tau) + t_{0i} c^*_{0\sigma}(\tau) c_{i\sigma}(\tau). \tag{2.26}$$

The action of the lattice without te site $i = 0$:

$$S^{(0)} = \int_0^\beta d\tau \Bigg(\sum_{i\neq 0,\sigma} c^*_{i\sigma}(\tau) \left[\frac{\partial}{\partial \tau} - \mu \right] c_{i\sigma}(\tau) - \sum_{ij\neq 0,\sigma} t_{ij} c^*_{i\sigma}(\tau) c_{i\sigma}(\tau) + U \sum_{i\neq 0} c^*_{i\uparrow}(\tau) c_{i\uparrow}(\tau) c^*_{i\downarrow}(\tau) c_{i\downarrow}(\tau) \Bigg) \tag{2.27}$$

We now define the thermodynamic average which is the trace over the system with the impurity removed, as below:

$$\langle A\rangle_{(0)} = \frac{1}{\mathcal{Z}^{(0)}} \int \prod_{i\neq 0,\sigma} Dc^*_{i\sigma} Dc_{i\sigma} A e^{-S^{(0)}} \tag{2.28}$$

where $\mathcal{Z}^{(0)}$ is the partition function of the impurity removed lattice. Thus, the full partition function $\mathcal{Z}$ with respect to ΔS is:

$$\mathcal{Z} = \mathcal{Z}^{(0)} \int \prod_{\sigma} Dc^*_{0\sigma} Dc_{0\sigma} e^{-S_0} \Bigg(1 - \int_0^\beta \langle \Delta S(\tau)\rangle_{(0)} d\tau + \frac{1}{2!}\int_0^\beta \int_0^\beta \langle \Delta S(\tau_1)\Delta S(\tau_2)\rangle_{(0)} d\tau_2 d\tau_1 + \ldots \Bigg) \tag{2.29}$$

where $\Delta S = \int_0^\beta d\tau \Delta S(\tau)$. In the fermionic system only the correlation functions $\langle \Delta S(\tau_1)\ldots \Delta S(\tau_n)\rangle_{(0)}$ with equal number of c and c^* are non-zero [49]. The second order term in Eq. (2.29) can be written as:

$$\begin{aligned} +\frac{1}{2!}\int_0^\beta \int_0^\beta \langle \Delta S(\tau_1)\Delta S(\tau_2)\rangle_{(0)} d\tau_2 d\tau_1 = \\ \frac{1}{2!}\int_0^\beta \int_0^\beta \sum_\sigma \sum_{j,k\neq 0} \big[t_{j0}t_{0k} \langle c^*_{j\sigma}(\tau_1) c_{k\sigma}(\tau_2)\rangle_{(0)} c_{0\sigma}(\tau_1) c^*_{0\sigma}(\tau_2) \\ + t_{0j}t_{k0} \langle c_{j\sigma}(\tau_1) c^*_{k\sigma}(\tau_2)\rangle_{(0)} c_{0\sigma}(\tau_1)^* c_{0\sigma}(\tau_2)\big] d\tau_2 d\tau_1 \end{aligned} \tag{2.30}$$

The above expression can be rewritten with the use of a one-particle correlation function, namely the Green's function of the lattice without the site 0

$$G^{(0)}_{jk\sigma}(\tau_1 - \tau_2) = \langle T_\tau c_{j\sigma}(\tau_1) c^*_{k\sigma}(\tau_2)\rangle_{(0)} \tag{2.31}$$

and takes the following form:

$$\begin{aligned} +\frac{1}{2!}\int_0^\beta \int_0^\beta \langle \Delta S(\tau_1)\Delta S(\tau_2)\rangle_{(0)} d\tau_2 d\tau_1 = \\ -\int_0^\beta \int_0^\beta \sum_\sigma \sum_{j,k\neq 0} t_{j0}t_{k0} G^{(0)}_{jk\sigma}(\tau_1 - \tau_2) c^*_{0\sigma}(\tau_1) c_{0\sigma}(\tau_2) d\tau_2 d\tau_1 \end{aligned} \tag{2.32}$$

Higher-order terms can be obtained similarly with the use of n-particle correlation functions. Note that in the expansion of partition function $\mathcal{Z}$ in Eq. (2.29) the terms of n-th order contain n factors of hopping amplitudes, and the non-trivial limit $d \to \infty$ is obtained by rescaling the hopping amplitudes. Finally, the effective local DMFT action would be:

$$S_{loc} = \int_0^\beta d\tau \left(\sum_\sigma c^*_{0\sigma}(\tau) \left[\frac{\partial}{\partial \tau} - \mu \right] c_{0\sigma}(\tau) + U c^*_{0\uparrow}(\tau) c_{0\uparrow}(\tau) c^*_{0\downarrow}(\tau) c_{0\downarrow}(\tau) \right) + \int_0^\beta \int_0^\beta \sum_\sigma \sum_{j,k\neq 0} t^*_{j0} t^*_{k0} G^{(0)}_{jk\sigma}(\tau_1 - \tau_2) c^*_{0\sigma}(\tau_1) c_{0\sigma}(\tau_2) d\tau_2 d\tau_1 \quad (2.33)$$

where the rescaled hopping amplitudes are denoted by t^*. We introduce the hybridization function:

$$\Delta_\sigma(\tau_1 - \tau_2) = \sum_{i,j\neq 0} t^*_{i0} t^*_{j0} G^{(0)}_{ij\sigma}(\tau_1 - \tau_2) \quad (2.34)$$

and define the so-called effective "Weiss field" $\mathcal{G}_\sigma$ for the HM as:

$$\mathcal{G}^{-1}_\sigma(\tau_1 - \tau_2) = -\left[\frac{\partial}{\partial \tau} - \mu \right] \delta(\tau_1 - \tau_2) - \Delta_\sigma(\tau_1 - \tau_2) \quad (2.35)$$

which allows us to express the DMFT local action in the following form (here the site $i = 0$ is omitted for readability):

$$S_{loc} = -\int_0^\beta \int_0^\beta \sum_\sigma c^*_\sigma(\tau_1) \mathcal{G}^{-1}_\sigma(\tau_1 - \tau_2) c_\sigma(\tau_2) d\tau_2 d\tau_1 + U \int_0^\beta d\tau c^*_\uparrow(\tau) c_\uparrow(\tau) c^*_\downarrow(\tau) c_\downarrow(\tau) \quad (2.36)$$

Eq. (2.36) shows that the action of the HM is identical to the action of a single site embedded in an effective field $\mathcal{G}^{-1}_\sigma$ plus the local Coulomb interaction on this site U. On the other hand, the effective Weiss field in Eq. (2.35) defines the full partition function and thus all information of the system, and $G^{(0)}_{ij\sigma}$ the Green's function of the original HM with one site removed. In addition, Eq. (2.36) creates a self-consistent relation, since the calculation

of the partition function $\mathcal{Z}$ now requires the knowledge of the Green's function and vice versa [49].

By applying the Fourier transform on Eq. (2.35), the Weiss field $\mathcal{G}_\sigma^{-1}$ takes a slightly simpler form:

$$\mathcal{G}_\sigma^{-1}(i\omega_n) = -i\omega_n + \mu - \Delta_\sigma(i\omega_n), \tag{2.37}$$

where

$$\Delta_\sigma(i\omega_n) = \sum_{i,j\neq 0} t_{i0}^* t_{j0}^* G_{ij\sigma}^{(0)}(i\omega_n) \tag{2.38}$$

Now we need the relation between the $G_{ij\sigma}^{(0)}$ the Green function with the site 0 removed and the full original lattice Green function $G_{ij\sigma}$, which is [49]:

$$G_{ij\sigma}^{(0)} = G_{ij\sigma} - G_{i0\sigma} G_{00\sigma}^{-1} G_{0j\sigma} \tag{2.39}$$

This relation enables us to express the local Green's function $G_{00\sigma} = G_\sigma$ by the dynamical Weiss mean field $\mathcal{G}_\sigma^{-1}$ in the form of a Dyson equation:

$$G_\sigma^{-1}(i\omega_n) = \mathcal{G}_\sigma^{-1}(i\omega_n) - \Sigma_\sigma(i\omega_n) = i\omega_n + \mu - \Delta_\sigma(i\omega_n) - \Sigma_\sigma(i\omega_n) \tag{2.40}$$

Then the original momentum-dependent lattice Green function $G_\sigma(k, i\omega_n)$ is given by:

$$G_\sigma(k, i\omega_n) = \frac{1}{i\omega_n + \mu - \varepsilon_k - \Sigma_\sigma(i\omega_n)} \tag{2.41}$$

and the local Green function:

$$G_\sigma(i\omega_n) = \frac{1}{N}\sum_k G_\sigma(k, i\omega_n) = \frac{1}{N}\sum_k \frac{1}{i\omega_n + \mu - \varepsilon_k - \Sigma_\sigma(i\omega_n)}, \tag{2.42}$$

where N is the number of points of the lattice. Finally,

$$\mathcal{G}_\sigma^{-1}(i\omega_n) = \Sigma_\sigma(i\omega_n) + G_\sigma^{-1}(i\omega_n) \tag{2.43}$$

the effective Weiss mean field equation is obtained [49].

It is very important to note that the interacting Green's function of the original lattice in Eq. (2.42) is still a momentum-dependent quantity which depends on the momentum through the dispersion ε_k of the non-interacting electrons. However, the DMFT corresponds to an effectively local problem in which the self-energy Σ_σ is a local quantity, equivalently, is a k-independent quantity.

The equations (2.36), (2.37), (2.40) and (2.43) form a set of self-consistent equations that can be solved iteratively. In order to find the interacting lattice Green's function, one starts with an initial guess for $\Sigma_\sigma(i\omega_n)$, which is usually zero, then using Eq. (2.43) one can obtain the Weiss field $\mathcal{G}_\sigma^{-1}$ and solve the corresponding local problem defined by the action S_{loc} in Eq. (2.36). Consequently, a new self-energy from the Dyson equation in Eq. (2.40) can be obtained. After convergence, one finds the correct Weiss field $\mathcal{G}_\sigma^{-1}$, that parametrizes the effective field surrounding a lattice site of the HM in $d \to \infty$, with the corresponding interacting Green's function G_σ and self-energy Σ_σ. At the end, the local interacting Green's function is equal to the momentum-averaged interacting lattice Green's function. Nevertheless, solving the local system is still complicated and in general cannot be performed analytically [49].

Having solved the DMFT equations and the local problem, we now ready to compare them to the AIM. The AIM consists of an impurity site embedded in a non-interacting bath, from which electrons can hop into the impurity site, interact via the local Coulomb repulsion and then hop back into the bath. In general, the Hamiltonian of the quantum impurity is consisting of three basic terms:

$$H_{QI} = H_{loc} + H_{hyb} + H_{bath} \tag{2.44}$$

where H_{loc} describes the impurity, where two electrons interact with the Coulomb potential. This local impurity Hamiltonian may be represented as a set of single-particle fermionic states labeled by quantum numbers $a = 1, ..., N$ (including both spatial and spin degrees of freedom):

$$H_{loc} = H^0_{loc} + H^I_{loc} \tag{2.45}$$

$$H^0_{loc} = \sum_{ab} E^{ab} c^\dagger_a c_b \tag{2.46}$$

$$H^I_{loc} = \sum_{pqrs} I^{pqrs} c^\dagger_p c^\dagger_q c_r c_s + ... \tag{2.47}$$

where the matrix E^{ab} denotes the bare energy level structure and I denotes electron-electron interactions. H_{bath} which describes the non-correlated electronic state, may be described as bands of itinerant electrons, each labeled by a one-dimensional momentum k or band energy ε_k and an index α (spin and orbital). So,

$$H_{bath} = \sum_{k\alpha} \varepsilon_{k\alpha} a^\dagger_{k\alpha} a_{k\alpha} \tag{2.48}$$

and H_{hyb} describes the hybridization (coupling) between the impurity and the bath. This mixing term which is characterized by a hybridization matrix V is equal to:

$$H_{hyb} = \sum_{k\alpha b} V^{\alpha b}_k \left(a^\dagger_{k\alpha} c_b + c^\dagger_b a_{k\alpha} \right) \tag{2.49}$$

although exchange couplings also arises:

$$H^{exchange}_{hyb} = \sum_{k_1 k_2 abcd} J^{abcd}_{k_1 K_2} \left(a^\dagger_{k_1 a} a_{k_2 b} + c^\dagger_c c_d \right) \tag{2.50}$$

like a spin exchange coupled to a bath of conduction electrons in the "Kondo problem" [50]. The paradigmatic quantum impurity model is the single-impurity Anderson model [38].

Since in this model, H_{loc} describes a single orbital, so the label a is spin-up (down), E^{ab} is a level energy ε_0, and the interaction term collapses to $Uc^{\dagger}_{\uparrow}c_{\uparrow}c^{\dagger}_{\downarrow}c_{\downarrow}$. Thus,

$$H_{AIM} = \sum_{\sigma} \varepsilon_0 c^{\dagger}_{\sigma} c_{\sigma} + U c^{\dagger}_{\uparrow} c_{\uparrow} c^{\dagger}_{\downarrow} c_{\downarrow} + \sum_{k\sigma} V_k \left(a^{\dagger}_{k\sigma} c_{\sigma} + c^{\dagger}_{\sigma} a_{k\sigma} \right) + \sum_{k\sigma} \varepsilon_k a^{\dagger}_{k\sigma} a_{k\sigma} \tag{2.51}$$

where $a^{\dagger}_{k\sigma}, a_{k\sigma}$ are the annihilation and creation operators for electrons in the bath. $c^{\dagger}_{k\sigma}, c_{k\sigma}$ are the annihilation and creation operators for the electrons on the impurity site. V_k which couples the impurity with the bath, corresponds to the annihilation of one electron in the bath and creation of one electron on the impurity site, and vice versa. U denotes the the Coulomb interaction on the impurity [41].

It was shown in [37] that AIM generates exactly the same effective action S_{AIM} as the Hubbard model in Eq. (2.36)

$$S_{AIM} = -\int_0^{\beta} \int_0^{\beta} \sum_{\sigma} c^{*}_{\sigma}(\tau_1) \mathcal{G}^{-1}_{\sigma}(\tau_1 - \tau_2) c_{\sigma}(\tau_2) d\tau_2 d\tau_1 + U \int_0^{\beta} d\tau c^{*}_{\uparrow}(\tau) c_{\uparrow}(\tau) c^{*}_{\downarrow}(\tau) c_{\downarrow}(\tau) \tag{2.52}$$

which the Weiss field is given by:

$$\mathcal{G}^{-1}_{\sigma}(\tau_1 - \tau_2) = -\left[\frac{\partial}{\partial \tau} - \mu \right] + \sum_k |V_K|^2 \left[\theta(\tau_1 - \tau_2) - n_F(\tilde{\varepsilon}_k) \right] \tag{2.53}$$

The Fourier transform of the Weiss field in Eq. (2.53) is:

$$\mathcal{G}^{-1}_{\sigma}(i\omega_n) = -i\omega_n + \tilde{\mu} - \sum_k \frac{|V_K|^2}{i\omega_n - \tilde{\varepsilon}_k} \tag{2.54}$$

Since the action S_{AIM} and S_{loc} are equivalent, we conclude that indeed the solution of the HM can be obtained by solving an AIM with the special choice of the Weiss field given by Eq. (2.43) [37].

Therefore, the lattice problem is mapping onto an embedded impurity problem self-consistently. The DMFT algorithm, as explained before, starts with a guess for the local

self energy $\Sigma_\sigma(i\omega_n)$ (usually zero). Then, the local lattice Green function $G_\sigma(i\omega_n)$ is calculated by using Eq. (2.42). Next, $\mathcal{G}_\sigma(i\omega_n)$ is computed which includes self-energy at all lattice sites except at the impurity site i, $\mathcal{G}_\sigma^{-1}(i\omega_n) = \Sigma_\sigma(i\omega_n) + G_\sigma^{-1}(i\omega_n)$. This quantity defines the site excluded bare Green function of a generalized AIM. We solve the impurity problem with some numerical technique, e.g., Continuous-Time Auxiliary (CT-AUX) field method, which produces $G_{imp}(i\omega_n)$, the Green function of the generalized AIM. Then using $\Sigma_\sigma(i\omega_n) = \mathcal{G}_\sigma^{-1}(i\omega_n) - G_{imp}^{-1}(i\omega_n)$, the new local self-energy is obtained which can be used in Eq. (2.42) to produce the new local Green's function (see Fig. 2.2). The iteration is continued until $G_\sigma(i\omega_n) = G_{imp}(i\omega_n)$ and the self-energy converges to the desired accuracy [51].

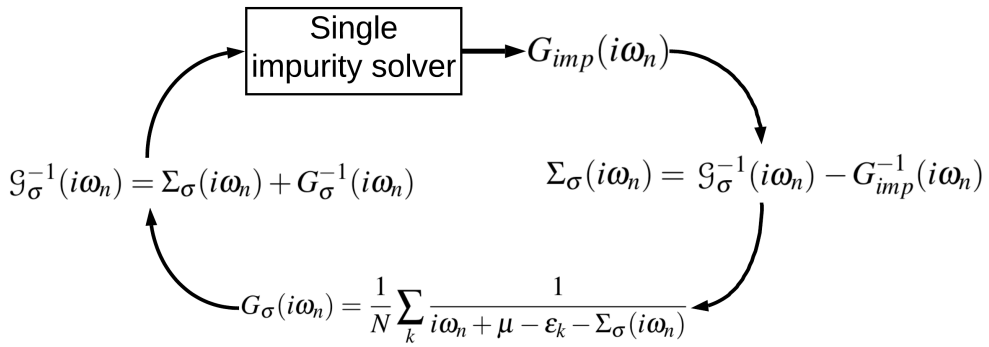

Figure 2.2 – Sketch of the DMFT algorithm.

In general, we derived the DMFT equations and described the ways to solve them by relating the effective field in $d \to \infty$ to the bath of an AIM. This method can be applied to all kinds of lattice systems for the HM for which the non-interacting dispersion or density of states is known. The DMFT itself is non-perturbative treatment of local interactions which is valid for the complete range of U and temperature T. It only relies on the ap-

proximation that $1/Z$ is small (Z is coordination number), which we assume is quite a good approximation for realistic systems.

2.2.4 Dynamical Cluster Approximation (DCA)

DMFT can be obtained by assuming a purely local self-energy even in finite dimensions. Although it has been shown that this approximation captures many key features of strongly correlated systems even in a finite-dimensional context, the DMFT has some obvious and significant restrictions. For instance, the only dynamical correlations present are those that are treated on a single site. Therefore, there are no nonlocal dynamical correlations. These are necessary, for example, to describe phases with explicitly nonlocal order parameters. But even phases with local order parameters (e.g., commensurate magnetism) will certainly be affected by the nonlocal dynamical correlations which are neglected by the DMFT. Besides, it was shown that the DMFT is not a conserving approximation [51].

An acceptable theory is needed which systematically incorporates nonlocal corrections to the DMFT. It must be able to responsible for fluctuations in the local environment self-consistently. It must be formulated in the way that becomes exact in the limit of large cluster sizes, and recover the DMFT when the cluster size equals to one. Also, it must be easily implementable numerically and preserve the translational and point-group symmetries of the lattice. There have been several efforts to formulate theories which satisfy these criteria. Among them, the dynamical cluster approximation (DCA) was proposed as an extension to the DMFT. In the DCA, the infinite lattice problem is reduced to a finite-sized cluster impurity (instead of a single impurity as in the DMFT) with periodic boundary conditions which are embedded into a self-consistent mean-field. [52].

In general, the DCA is constructed in analogy with the DMFT. Both of these two approximations can be interpreted as a coarse graining procedure of the Greens function and self energy. In the DMFT, as illustrated in Fig. (2.3) for a two-dimensional lattice, mapping the original lattice problem to a self-consistent impurity problem is equivalent to averaging the Green functions, which are used to calculate the self-energy, over the points in the Brillouin zone. An important consequence of this averaging is leading to local (momentum-independent) self-energy and the irreducible vertices of the lattice [52]. This

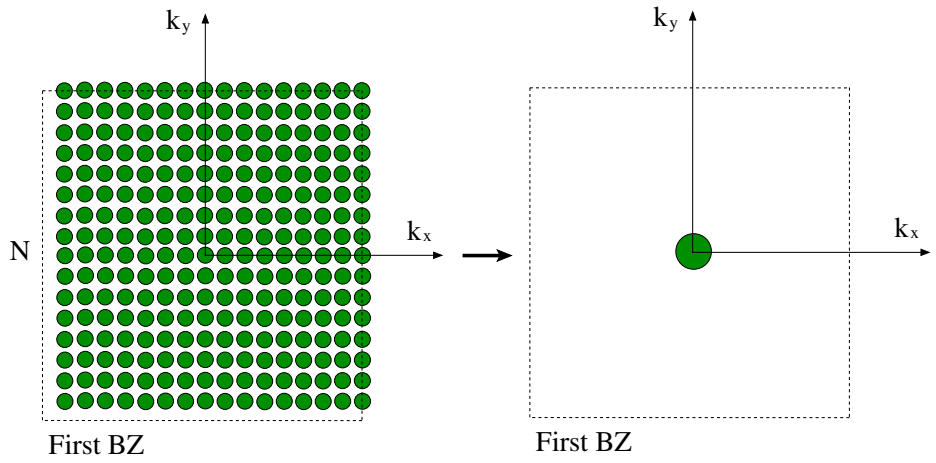

Figure 2.3 – Illustration of coarse graining in the DMFT. *Left*: all lattice propagators are averaged over the points in the first Brillouin zone. *Right*: mapping the lattice problem to a single point in reciprocal space. Since the real space and reciprocal space are equivalent, this maps the lattice problem to an impurity embedded within a host.

coarse-graining is exact in the limit of infinite dimensions. For Hubbard like models, the Laue function Δ which expresses the momentum conservation at each vertex characterizes the properties of a bare vertex. In a conventional diagrammatic approach:

$$\Delta(k_1,k_2,k_3,k_4) = \sum_r e^{[ir.(k_1+k_2-k_3-k_4)]} = N\delta_{k_1+k_2,k_3+k_4} \tag{2.55}$$

where k_1, k_2 are the momenta entering and k_3, k_4 are the momenta leaving each vertex through its legs of G. However, in the limit of infinite-dimensions $D \to \infty$ the Laue function reduces to [53]:

$$\Delta_{D\to\infty}(k_1,k_2,k_3,k_4) = 1 + \mathcal{O}(1/D) \tag{2.56}$$

The DMFT supposes the Laue function $\Delta_{DMFT}(k_1,k_2,k_3,k_4) = 1$, even in the finite dimensions. Thus, DMFT neglects conservation of momentum at internal vertices. Therefore we can freely sum over the internal momentum labels of each Green function leg. In other words, the momentum-dependent contributions is collapsed, and only local terms remain. On the other hand, in the DCA, momentum conservation and nonlocal corrections are restored systematically; thus, in the DCA, the reciprocal space of the lattice (Fig. 2.4) which contains N points is divided into N_c cells of identical linear size Δk. In the coarse-graining

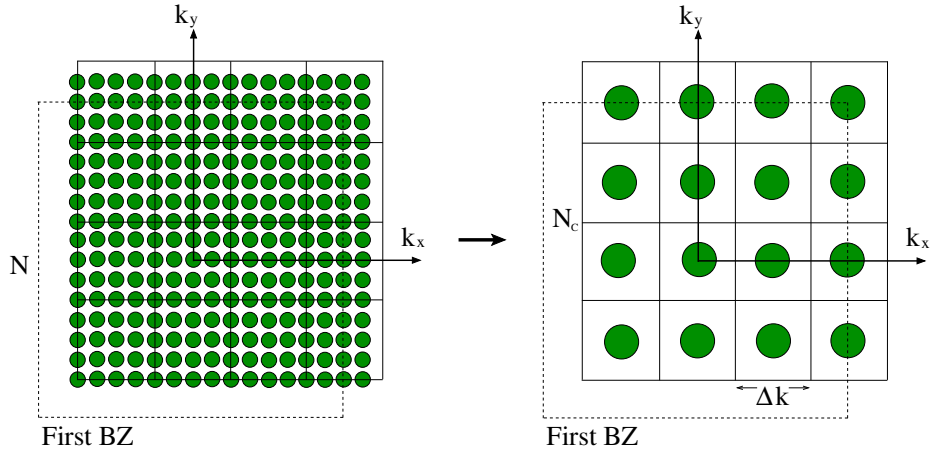

Figure 2.4 – Illustration of the coarse graining in the DCA. *Left*: all lattice propagators are averaged over the points within each cell in the first Brillouin zone. *Right*: mapping the lattice problem to a small cluster defined by the centers of the cells embedded within a host.

transformation, the Green's function is averaged within each cell. In the $N_c = 1$ case, the

lattice problem is mapped to an impurity problem (DMFT), and in $N_c > 1$, the nonlocal correction length $\approx \pi/\Delta k$ to the DMFT is introduced [52].

2.2.4.1 Diagrammatic Derivation of DCA

A microscopic diagrammatic derivation of the DCA can illustrate the coarse-graining procedure and the relationship of the DCA to the DMFT. In DCA, the momentum conservation is systematically restored at internal vertices which is relinquished by the DMFT. First the Brillouin zone is divided into N_c cells of size Δk (with $N_c = L^D$ and $\Delta k = 2\pi/L$), then each cell is centered on a cluster momentum $\mathbf{K}$ (see Fig. 2.5). Momentum is conserved

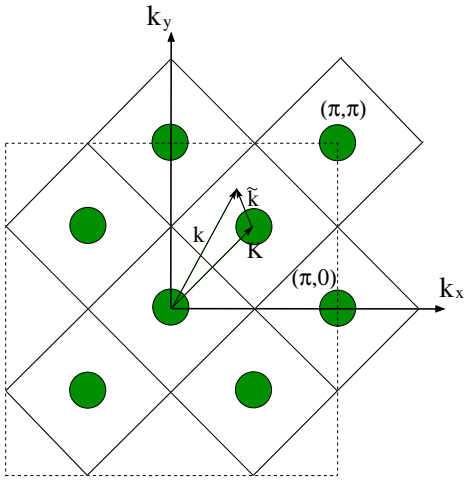

Figure 2.5 – Illustration of coarse graining cells for $N_c = 8$ that divide the first Brillouin Zone. Each cell is centered on a cluster momentum $\mathbf{K}$, and a generic momentum in the zone such as k is mapped to the nearest cluster momentum $\mathbf{K} = M(k)$ so that $\tilde{k} = k - \mathbf{K}$ remains in the cell around $\mathbf{K}$.

for momentum transfers between cells, i.e., for momentum transfers larger than Δk, but momentum conservation is neglected for momentum transfers inside a cell, i.e., less than

Δk. This condition can be obtained by using the Laue function [51]:

$$\Delta_{DCA}(k_1,k_2,k_3,k_4) = N_c \delta_{M(k_1)+M(k_2),M(k_3)+M(k_4)} \tag{2.57}$$

where $M(k)$ is a function which maps k into the cluster momentum $\mathbf{K}$ of the cell containing k (see Fig. 2.5). Note that with this choice for the Laue function, the exact result, Eq. (2.55), and the DMFT result, Eq. (2.56) is recovered when $N_c \to N$ and $N_c = 1$ respectively. Also, with this choice of the Laue function, the summation of momentum over the cell can give the momenta of each internal leg, so that each internal leg $G(k)$ is replaced by the coarse-grained Green's function $\bar{G}[M(k)]$ which is defined by:

$$\bar{G}(\mathbf{K}, i\omega_n) = \frac{N_c}{N} \sum_{\tilde{k}} G(\mathbf{K}+\tilde{k}, i\omega_n) \tag{2.58}$$

where N denotes the number of points of the lattice, N_c is the number of cluster $\mathbf{K}$ points, and the $\tilde{k}$ summation runs over the momenta of the cell about the cluster momentum $\mathbf{K}$ (see Fig. 2.5). In DCA, the cluster self-energy $\Sigma_c(\mathbf{K}, i\omega_n)$ is assumed to give the real lattice self-energy for values of the lattice momenta inside the cells around the cluster momenta $\Sigma_c(\mathbf{K}, i\omega_n) \approx \Sigma(\mathbf{K}+\tilde{k}, i\omega_n)$. This assumption is justified if the momentum dependence of the self-energy of the real system is sufficiently weak, which means that $\Sigma(\mathbf{K}+\tilde{k}, i\omega_n) \approx \Sigma(\mathbf{K}, i\omega_n)$. Therefore, the lattice self-energy is well approximated by the cluster self-energy. Next, using the same approximation, the cluster self-energies can be equated with the coarse-grained averages of the lattice self-energies over these momentum cells around the cluster momenta. Thus, for the self-energy,

$$\Sigma_c(\mathbf{K}, i\omega_n) = \bar{\Sigma}(\mathbf{K}, i\omega_n) = \frac{N_c}{N} \sum_{\tilde{k}} \Sigma(\mathbf{K}+\tilde{k}, i\omega_n) \tag{2.59}$$

the corresponding cluster Green's function $G_c(\mathbf{K}, i\omega_n)$ is given by the coarse grained average of the real lattice Green's function,

$$G_c(\mathbf{K}, i\omega_n) = \bar{G}(\mathbf{K}, i\omega_n) = \frac{N_c}{N} \sum_{\tilde{k}} \frac{1}{i\omega_n - \varepsilon_k + \mu - \Sigma_c(\mathbf{K}, i\omega_n)} \tag{2.60}$$

where ε_k is the dispersion for the non interacting lattice problem and μ is the chemical potential [51].

The bare Green's function or cluster-excluded Green's function which is the coarse-grained Green's function with correlations on the cluster excluded is determined by the Dyson equation on the cluster:

$$\mathcal{G}^{-1}(\mathbf{K}, i\omega_n) = \bar{G}^{-1}(\mathbf{K}, i\omega_n) + \Sigma_c(\mathbf{K}, i\omega_n) \tag{2.61}$$

Since $\Sigma_c(\mathbf{K}, i\omega_n)$ is unknown, it must be determined self-consistently, starting from an ini-

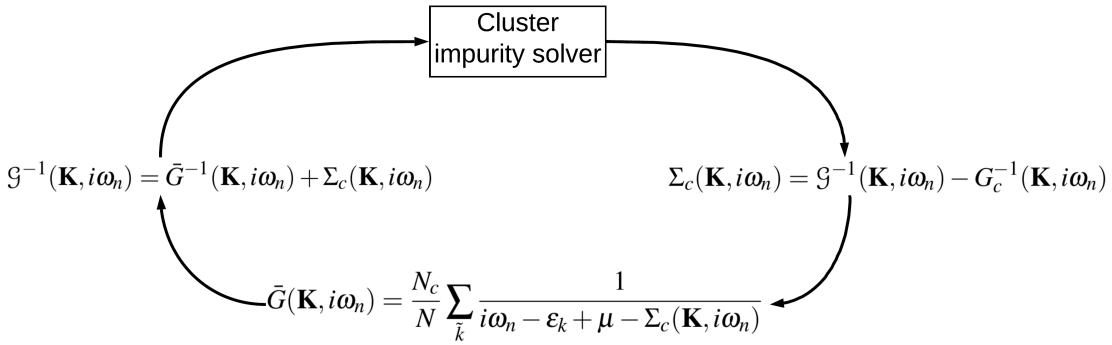

Figure 2.6 – Sketch of the DCA algorithm.

tial guess, usually zero. This guess is used to calculate the coarse-grained Green's function $\bar{G}(\mathbf{K}, i\omega_n)$ using Eq. (2.60). The bare Green's function $\mathcal{G}(\mathbf{K}, i\omega_n)$ is then calculated by Eq. (2.61), and used to initialize the cluster problem solver calculation. The solver produces

the cluster Green's function $G_c(\mathbf{K}, i\omega_n)$ through which the cluster self-energy is calculated:

$$\Sigma_c(\mathbf{K}, i\omega_n) = \mathcal{G}^{-1}(\mathbf{K}, i\omega_n) - G_c^{-1}(\mathbf{K}, i\omega_n) \tag{2.62}$$

Again by using Eq. (2.60), the new $\bar{G}(\mathbf{K}, i\omega_n)$ is calculated, and the iteration is continued until $\bar{G}(\mathbf{K}, i\omega_n) = G_c(\mathbf{K}, i\omega_n)$ and the self-energy converges to the desired accuracy. The self-consistency loop for the DCA is shown in Fig. 2.6.

2.2.5 Impurity Solver-Continuous Time Quantum Monte Carlo

As explained in Sec. 2.2.3.1, since the Hamiltonian of the impurity model (Eq. 2.51) does not carry spatial dependency, it may look simple. Nonetheless, this model is still believed to be analytically intractable due to the presence of a kinetic and a non-separable two-particle interaction terms. There is a plethora of state-of-the-art numerical methods for solving the Anderson model at finite temperature including continuous-time quantum Monte Carlo (CT-QMC) methods and second-order approximation. We showed that at high temperature and weak interaction, the Green's function obtained by both methods are in good agreement with each other. However, by increasing the interaction strength the Green's functions start to differ. The second-order approximation as impurity solver is fully explained in Appendix A.

Prior to the development of CT-QMC methods, the Hirsch-Fye quantum Monte Carlo method [42] was the principal impurity solver. Hirsch-Fye method discretizes the interval $[0, \beta)$ in the imaginary-time functional integral into M equally spaced time slices so that $\Delta\tau = \beta/M$. Then the method applies a discrete Hubbard-Stratonovich transformation on each time slice i. The Hubbard-Stratonovich transformation, which is required to decouple

the interactions, for the single Anderson model is:

$$e^{-\Delta\tau U[n_\uparrow n_\downarrow - (\frac{n_\uparrow + n_\downarrow}{2})]} = \frac{1}{2}\sum_{s_i=\pm 1} e^{\lambda s_i (n_\uparrow - n_\downarrow)} \tag{2.63}$$

where $\lambda = arcosh[exp(\frac{1}{2}\Delta\tau U)]$ and $\{s_i\}$ are Ising variables. The problem, finally, becomes the sampling of the trace over the 2^M-dimensional space of the s_i. Besides the difficulty of choosing the equally spaced time discretization, the most fundamental difficulty which limits the Hirsch-Fye method power is that for interactions other than the simple one-orbital Hubbard model the Hubbard-Stratonovich fields proliferate and even can be complex so sampling the space of auxiliary fields becomes prohibitively hard. Since the discretization errors are large, a very small $\Delta\tau$ and a precise extrapolation of the results to $\Delta\tau = 0$ are required. Hence, methods which do not involve an explicit time discretization would be needed [41].

The Hamiltonian in the CT-QMC methods is split into two parts labeled by a and b, $H = H_a + H_b$, and the partition function $\mathcal{Z} = e^{-\beta H}$ in the interaction representation is written with respect to H_a and is expanded in powers of H_b, thus:

$$\mathcal{Z} = TrT_\tau e^{-\beta H_a} exp\Big[-\int_0^\beta d\tau H_b(\tau)\Big] = \sum_k (-1)^k \int_0^\beta d\tau_1 ... \int_{\tau_{k-1}}^\beta d\tau_k \times Tr[e^{-\beta H_a} H_b(\tau_k) H_b(\tau_{k-1}) ... H_b(\tau_1)] \tag{2.64}$$

where T_τ is the time ordering operator. The sampling over all orders k, all topologies of the paths and diagrams, and all times $\tau_1, ..., \tau_k$ in the calculation, is done using diagrammatic Monte Carlo methods [54] and the trace evaluates to a number. Since the method is based on continuous time, time-discretization errors do not have to be controlled. Besides, from the spectrum of the perturbation term bounded from above, the contributions of large orders are decreased by the factor $1/k!$; therefore, the sampling process does not run off to infinite

order, and the diagram order does not need to be truncated.

Therefore, in general, CT-QMC is based on expanding the partition function. There are four types of expansion in the impurity-model context: CT-HYB (hybridization expansion), CT-INT (interaction expansion), CT-AUX (auxiliary field expansion), and CT-J (expansion for Kondo-like problems). CT-INT and CT-AUX are both variations of an "interaction expansion" and these two methods are most suited to Hubbard-like models with a single local density-density interaction. They are sometimes referred to as weak-coupling expansions because they are restricted to weak interactions. In CT-INT and CT-AUX much larger systems can be treated because the scaling with the number of impurity orbitals is not exponential [41].

2.2.5.1 Monte Carlo basics: Sampling, Markov Chains, and the Metropolis Algorithm

In the CT-QMC methods, we are facing with the issue of evaluating sums over phase spaces or configuration spaces denoted by $\mathcal{C}$ which is typically of a very high dimension. The partition function $\mathcal{Z}$ is written as an integral over configurations $\mathbf{x} \in \mathcal{C}$ with weight $p(\mathbf{x})$:

$$\mathcal{Z} = \int_{\mathcal{C}} d\mathbf{x} p(\mathbf{x}) \tag{2.65}$$

$\mathbf{x}$ in the quantum problems represents a particular term in a diagrammatic partition function expansion. The expectation value of a quantity A is given by the distribution $\rho(\mathbf{x})$ and weight $p(\mathbf{x})$:

$$\langle A \rangle = \frac{\langle A(p/\rho) \rangle_\rho}{\langle p/\rho \rangle_\rho} \tag{2.66}$$

Multi-dimensional integrals with general distributions such as Eqs. (2.65) and (2.66) are properly sampled by generating configurations using a "Markov process" which is fully

characterized by a transition matrix $W_{\mathbf{xy}}$. The matrix $W_{\mathbf{xy}}$ determines the probability going from state $\mathbf{x}$ to state $\mathbf{y}$ in one step of the process. Markov process starts with an arbitrary distribution and converges exponentially to a stationary distribution $p(\mathbf{x})$ if the following two conditions are satisfied:

- Ergodicity: any configuration $\mathbf{x}$ can be obtained from any other configuration $\mathbf{y}$ in a finite number of Markov steps.

- Balance: Stationarity requires that the distribution $p(\mathbf{x})$ fulfills the balance condition,

$$\int_{\mathcal{C}} d\mathbf{x} p(\mathbf{x}) W_{\mathbf{xy}} = p(\mathbf{y}) \tag{2.67}$$

  where $p(\mathbf{x})$ is a left eigenvector of $W_{\mathbf{xy}}$. Usually a sufficient but not necessary *detailed balance* condition is used instead of the balance condition,

$$\frac{W_{\mathbf{xy}}}{W_{\mathbf{yx}}} = \frac{p(\mathbf{y})}{p(\mathbf{x})} \tag{2.68}$$

The "Metropolis-Hastings" algorithm [55, 56] is the first and still most widely used algorithm that satisfies detailed balance. By introducing the proposed probability $W_{\mathbf{xy}}^{prop}$ and the accepted probability $W_{\mathbf{xy}}^{acc}$ which show the update from a configuration $\mathbf{x}$ to a new configuration $\mathbf{y}$, the transition matrix gets the following form:

$$W_{\mathbf{xy}} = W_{\mathbf{xy}}^{prop} W_{\mathbf{xy}}^{acc} \tag{2.69}$$

By using the Metropolis-Hastings acceptance rate which is:

$$W_{\mathbf{xy}}^{acc} = min[1, R_{\mathbf{xy}}] \tag{2.70}$$

the detailed balance condition (Eq. 2.68) is satisfied. $R_{\mathbf{xy}}$ in Eq. (2.70) is the acceptance ratio and is given by:

$$R_{\mathbf{xy}} = \frac{p(\mathbf{y}) W_{\mathbf{yx}}^{prop}}{p(\mathbf{x}) W_{\mathbf{xy}}^{prop}} \tag{2.71}$$

and $R_{\mathbf{yx}} = 1/R_{\mathbf{xy}}$ [41].

2.2.5.2 Diagrammatic Monte Carlo Method: The Sampling of Path Integrals

Diagrammatic expansion of partition function as a sum of integrals in the general form:

$$\mathcal{Z} = \sum_{k=0} \sum_{\gamma \in \Gamma_k} \int_0^\beta d\tau_1 ... \int_{\tau_{k-1}}^\beta d\tau_k w(k, \gamma, \tau_1, ..., \tau_k) \tag{2.72}$$

has the form of Eq. (2.65) where the individual configurations **x** is:

$$\mathbf{x} = (k, \gamma, (\tau_1, ..., \tau_k)) \tag{2.73}$$

and the weight:

$$p(\mathbf{x}) = w(k, \gamma, \tau_1, ..., \tau_k) d\tau_1 ... d\tau_k \tag{2.74}$$

Here k is the expansion order, $\gamma \in \Gamma_k$ contains the discrete variables, such as the topology of the diagram, orbital, lattice site, and auxiliary spin indices associated with the interaction vertices, and $\tau_1, ..., \tau_k \in [0, \beta)$ are the times of the k vertices in the configuration. To illustrate the sampling of the Monte Carlo in such continuous-time partition function expansions, the partition function in simple form is being considered:

$$\mathcal{Z} = \sum_{k=0} \int_0^\beta d\tau_1 \int_0^\beta d\tau_2 ... \int_{\tau_{k-1}}^\beta d\tau_k w(k) \tag{2.75}$$

The probability distribution of an expansion order k with vertices at times $\{\tau_j\}$ is:

$$p(k, (\tau_1, ..., \tau_k)) = w(k) \prod_{i=1}^{k} d\tau_i \tag{2.76}$$

In diagrammatic Monte Carlo, "updates" realize transitions between configurations x and y. Updates in diagrammatic Monte Carlo codes typically involve:

(i) updates that increase the order k: inserting an additional vertex at a time τ.

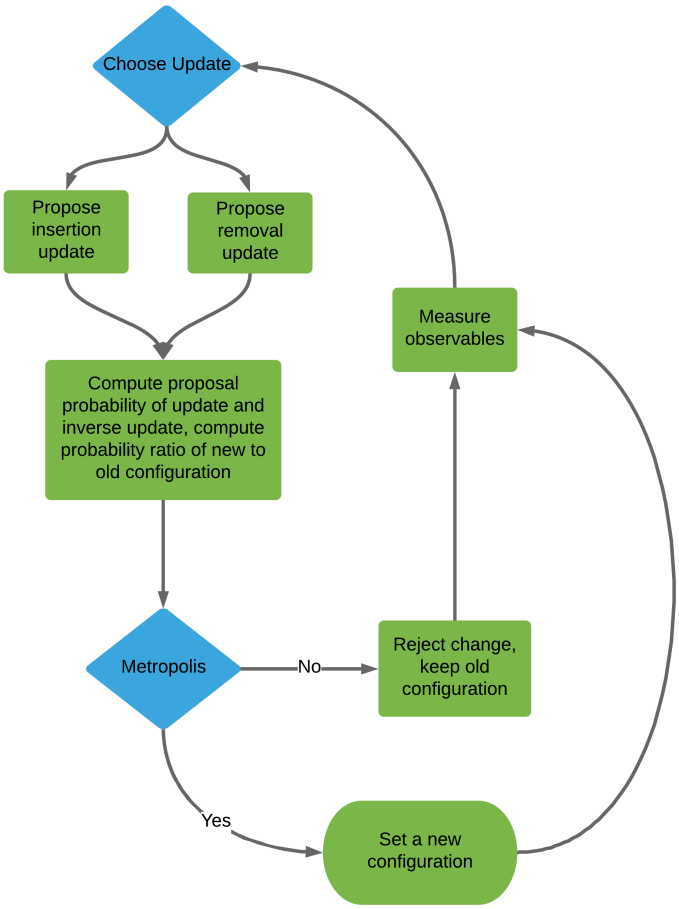

Figure 2.7 – Sketch of the continuous-time quantum Monte Carlo algorithm.

(ii) updates that decrease the order k: removing a vertex τ_j.

Ergodicity requires these insertion and removal updates. By removing all the existing vertices and then inserting new ones any configuration from another one can be reached. The general scheme of diagrammatic Monte Carlo algorithms is shown in Fig. 2.7 [41].

2.2.5.3 Continuous-Time Auxiliary Field CT-AUX

CT-AUX method presented here is a formulation applicable to both single and cluster impurity problems [41, 57]. CT-AUX algorithm is based on an interaction expansion accom-

panied with an auxiliary-field decomposition of the interaction vertices. CT-AUX may be viewed as an optimal Hirsch-Fye algorithm with the advantages of a continuous-time method. It was shown that this method in the case of the single-band Hubbard model is equivalent to the weak-coupling algorithm [58] and is the method of choice for large cluster simulations [41].

As is mentioned before, continuous-time solvers are starting with the expanding of the partition function. The partition function is $\mathcal{Z} = Tre^{-\beta(H_0+H_U)}$ and a nonzero constant K is added to H_U:

$$H_U = U\sum_i^{N_c}\Big(n_{i\uparrow}n_{i\downarrow} - \frac{n_{i\uparrow}+n_{i\downarrow}}{2}\Big) - \frac{K}{\beta} \tag{2.77}$$

$$H_0 = H_{AIM} - H_U + K/\beta \tag{2.78}$$

Note that N_c is a cluster sites in a cluster impurity problem. Thus, the partition function:

$$\mathcal{Z} = Tr\Big[e^{-\beta H_0}Tre^{\int d\tau\{K/\beta - U\sum_i^{N_c}[n_{i\uparrow}n_{i\downarrow} - (n_{i\uparrow}+n_{i\downarrow})/2]\}}\Big] \tag{2.79}$$

If the exponential is expanded in powers of H_U and the auxiliary-field decomposition is applied [59]:

$$1 - \frac{\beta U}{K}\sum_i^{N_c}\Big(n_{i\uparrow}n_{i\downarrow} - \frac{n_{i\uparrow}+n_{i\downarrow}}{2}\Big) = \frac{1}{2N_c}\sum_{i,s_i=\pm 1} e^{\gamma s_i(n_{i\uparrow}-n_{i\downarrow})} \tag{2.80}$$

$$cosh(\gamma) = 1 + \frac{U\beta N_c}{2K} \tag{2.81}$$

the partition function gets the following form:

$$\mathcal{Z} = \sum_{k=0}^{\infty}\sum_{s_1,\ldots,s_k=\pm 1}\int_0^\beta d\tau_1 \ldots \int_{\tau_{k-1}}^\beta d\tau_k\Big(\frac{K}{2\beta N_c}\Big)^k \mathcal{Z}_k(\{s_k,\tau_k,x_k\}) \tag{2.82}$$

where,

$$\mathcal{Z}_k(\{s_i,\tau_i,x_i\}) \equiv Tr\prod_{i=k}^{1} e^{-\Delta\tau_i H_0} e^{s_i\gamma(n_{x_i\uparrow}-n_{x_i\downarrow})} \tag{2.83}$$

with $\Delta\tau_i \equiv \tau_{i+1}-\tau_i$ for $i<k$ and $\Delta\tau_k \equiv \beta-\tau_k+\tau_1$. Finally, following the derivation done in [57], we obtain:

$$\frac{\mathcal{Z}_k(\{s_i,\tau_i,x_i\})}{\mathcal{Z}_0} = \prod_{\sigma=\uparrow,\downarrow} detN_\sigma^{-1}(\{s_i,\tau_i,x_i\}) \tag{2.84}$$

where $\mathcal{Z}_0 = Tre^{-\beta H_0}$ and,

$$N_\sigma^{-1}(\{s_i,\tau_i,x_i\}) \equiv e^{V_\sigma^{\{s_i\}}} - G_{0\sigma}^{\{\tau_i,x_i\}}\left(e^{V_\sigma^{\{s_i\}}}-1\right) \tag{2.85}$$

$$e^{V_\sigma^{\{s_i\}}} \equiv \left(e^{\gamma(-1)^\sigma s_1},...,e^{\gamma(-1)^\sigma s_k}\right) \tag{2.86}$$

with $(-1)^\uparrow \equiv 1$, $(-1)^\downarrow \equiv -1$ and $(G_{0\sigma}^{\{\tau_i,x_i\}})_{ij} = \mathcal{G}^0_{x_iX_j,\sigma}(\tau_i-\tau_j)$ for $i\neq j$, $(G_{0\sigma}^{\{\tau_i,x_i\}})_{ij} = \mathcal{G}^0_{x_iX_j,\sigma}(0^+)$. Therefore, the algorithm is formulated in terms of a matrix N_σ instead of G [41,57].

The partition function Eq. (2.82) in the CT-AUX algorithm includes a sum over expansion orders k up to infinity, discrete sum over auxiliary fields spins s and sites x, and a k-dimensional time-ordered integral in the interval $[0,\beta)$, so we can use the sampling scheme of Sec. 2.2.5.2. Note that, in addition to the imaginary-time locations of the interaction vertices, the auxiliary spins s_j associated with each vertex are sampled. So, the configuration space $\mathcal{C}$ in Eq. (2.65) is given by:

$$\mathcal{C} = \{\{\},\{(s_1,\tau_1)\},\{(s_1,\tau_1),(s_2,\tau_2)\},...,\{(s_1,\tau_1),...,(s_k,\tau_k),...\} \tag{2.87}$$

where the $s_j = \pm 1$ are auxiliary Ising spins, k is the expansion or diagram order, and $\tau_1<\tau_2<...<\tau_k$ are continuous variables between 0 and β. Fig. 2.8, which is for orders

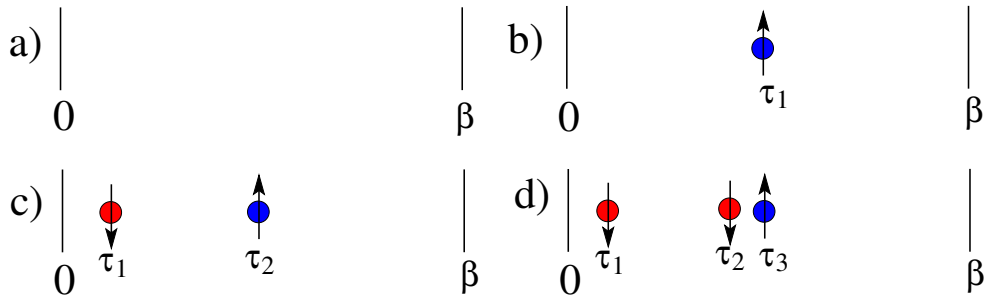

Figure 2.8 – Pictorial representation of configurations $\{(s_j, \tau_j)\} \in \mathcal{C}$ that occur within the CT-AUX algorithm. Diagrams for orders zero through three. The circles represent imaginary times at which the interactions take place. In CT-AUX algorithm, an auxiliary spin s_j(represented here by the arrows) needs to be sampled in addition to the imaginary time location τ_j of a vertex.

zero through three, shows the configurations $\{(s_j, \tau_j)\} \in \mathcal{C}$ that occur within the CT-AUX algorithm. Each configuration contributes some value to the whole partition function. Updates starts with spin-flip updates at constant order which are fast to compute:

$$[(s_1, \tau_1), ..., (s_j, \tau_j), ..., (s_k, \tau_k)] \Rightarrow [(s_1, \tau_1), ..., (-s_j, \tau_j), ..., (s_k, \tau_k)] \tag{2.88}$$

and then insertion and removal updates is used as is described in Sec. 2.2.5.2. Fig. 2.9 shows an insertion and removal update within the CT-AUX. Using Eq. (2.84), the proba-

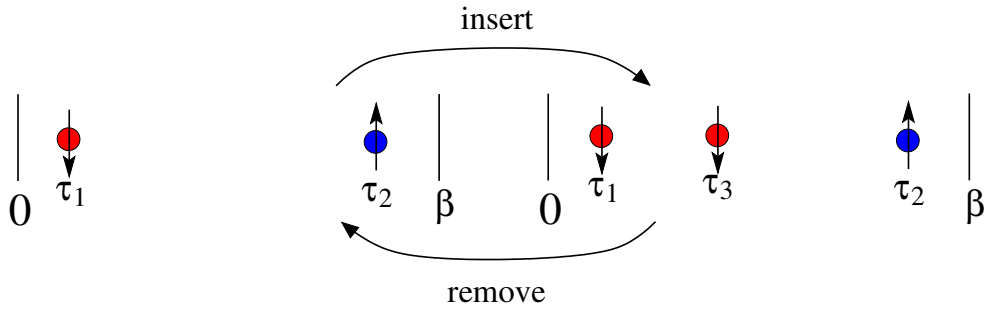

Figure 2.9 – Pictorial representation of an insertion and removal update within the CT-AUX algorithm.

bility density ratios of the two configurations:

$$R = \frac{P(\mathbf{y})}{P(\mathbf{x})} = \frac{\prod_{\sigma} detN_{\sigma}^{-1}(\{s_i^{'}, \tau_i^{'}, x_i^{'}\})}{\prod_{\sigma} detN_{\sigma}^{-1}(\{s_i, \tau_i, x_i\})} \tag{2.89}$$

For ergodicity it is sufficient for vertex insertion updates from configuration $\mathbf{x} = (\{s_i, \tau_i, x_i\})$ to configuration $\mathbf{y} = (\{s_i^{'}, \tau_i^{'}, x_i^{'}\})$ to be balanced by removal updates. By picking a random time in the interval $[0, \beta)$, a random site, and a random direction for spin, the proposal probability would be:

$$W_{\mathbf{xy}}^{prop} = \frac{1}{2N_c}\frac{d\tau}{\beta} \tag{2.90}$$

and the proposal probability of removing a spin,

$$W_{\mathbf{yx}}^{prop} = \frac{1}{k+1} \tag{2.91}$$

Therefore, following Eq. (2.71), the probability density ratios gets the below form [41].

$$R_{\mathbf{xy}} = \frac{K}{k+1}\frac{detN_{\uparrow}(\mathbf{y}) + detN_{\downarrow}(\mathbf{y})}{detN_{\uparrow}(\mathbf{x}) + detN_{\downarrow}(\mathbf{x})} \tag{2.92}$$

Measurement of the Green's function $G_{pq,\sigma}(\tau, \tau')$ for cluster sites p and q and spin σ, starts with adding two additional noninteracting spins $s = s' = 0$ to Eq. (2.83) at any arbitrary time τ and τ'. Thus, the Green's function is obtained (the corresponding matrices of size n+2 is denoted with a tilde)

$$G_{pq,\sigma}(\tau, \tau') = \frac{1}{\mathcal{Z}} \sum_{k \geq 0} \left(\frac{K}{2\beta N_c}\right)^k \sum_{s_i = \pm 1, 1 \leq i \leq k} \int_0^{\beta} d\tau_1 ... \int_{\tau_{k-1}}^{\beta} d\tau_k \times \mathcal{Z}_k(\{s_i, \tau_i, x_i\}) \tilde{G}_{pq,\sigma}^{\{s_i, \tau_i, x_i\}}(\tau, \tau') \tag{2.93}$$

where $\tilde{G}_{pq,\sigma}^{\{s_i, \tau_i, x_i\}} = \tilde{N}_{\sigma, pr}(\{s_i, \tau_i, x_i\}) \tilde{G}_{0, rq, \sigma}^{\{\tau_i\}}$. Since $s = s' = 0$:

$$\tilde{G}_{pq,\sigma}^{\{s_i, \tau_i, x_i\}}(\tau, \tau') = \mathcal{G}_{pq,\sigma}^{0}(\tau, \tau') + \sum_{l,m=1}^{k} \mathcal{G}_{px_l,\sigma}^{0}(\tau, \tau_l) M_{lm} \mathcal{G}_{x_m q,\sigma}^{0}(\tau_m, \tau') \tag{2.94}$$

$$M_{lm} = [(e^{V_\sigma^{\{s_i\}}} - 1)N_\sigma(\{s_i, \tau_i, x_i\})]_{lm} \tag{2.95}$$

Finally, by applying Fourier transform to the above expression, a measurement formula in frequency space is obtained [41]:

$$\tilde{G}_{pq}(i\omega_n) = \mathcal{G}^0_{pq}(i\omega_n) - \sum_{lm} \frac{\mathcal{G}^0_{pl}(i\omega_n)\mathcal{G}^0_{mq}(i\omega_n)}{\beta} e^{i\omega_n\tau_l} M_{lm} e^{-i\omega_n\tau_m} \tag{2.96}$$

2.3 Numerical Calculation

2.3.1 ALPSCore

The DMFT, DCA and the CT-AUX codes described in Sec. 2.2 are built on an updated version of the core libraries of ALPS (Algorithms and Libraries for Physics Simulations) also known as ALPSCore libraries [60,61]. The ALPS project is an C++ open source effort aiming at providing a collection of physics libraries and applications with high-end simulation codes for lattice models and strongly correlated electron systems. The ALPS libraries by reducing the users time and effort to develop and testing complex scientific applications, provide the well-documented components for numerical simulations of condensed matter systems, the applications, and computational algorithms to a non-expert community.

In this work we used the main ALPS Libraries known as ALPSCore libraries which provide physical insights into many subfields of condensed matter including nonequilibrium dynamics [62], CT-QMC [57, 63], LDA+DMFT materials simulations [64], and cuprate superconductivity [65]. Later versions of the code is available from the main site, http://alpscore.org, together with tutorials, and examples. Development versions of the library are available from the public Git repository at https://github.com/ALPSCore/ALPSCore.

2.3.2 Compute Canada

Compute Canada and their regional partner organizations including ACENET, Compute Ontario, Calcul Québec, and WestGrid, by deploying cutting-edge advanced research computing (ARC) systems, storage and software solutions, accelerate the research and innovation. They provide necessary ARC services and infrastructure for Canadian researchers and their collaborators in academia and industry. Also, Compute Canada's world-class experts in universities and research institutions across the country provide direct support to research teams. Compute Canada is an ambassador for Canadian excellence in advanced research computing nationally and internationally.

The present work done using resources provided by Calcul Québec organization. We used servers "Mp2" and "Mp2b" which are the sub-system of "Mammouth Parallel 2" cluster. Let us here to mention that the Mp2b is re-configured following Compute Canada standards. A detailed information about Calcul Québec and the Mp2 is available at `https://wiki.calculquebec.ca/w/Connecting_and_transferring_files#tab=tab7`, and the Mp2b at `https://wiki.ccs.usherbrooke.ca/Mammouth-Mp2b`.

Chapter 3

Results

Since we aim to find the phase diagram of the system, we do our calculations for $1 \leqslant U \leqslant 11$, $2 \leqslant \beta \leqslant 10$ both with the step of 0.5, and $0.0 \leqslant t_f \leqslant 1.0$ with the step of 0.1. In addition, in the results relevant to DCA, we increase the system size N from 1 to 8 and 16. Since CPU usage necessary to receive well converged, statistically sound results scales as U^3, β^3 and N^3, our numerical investigation from the point of view of the computational efforts is expensive.

3.1 Green's Function and Self-Energy Using DMFT

In DMFT, a set of self-consistency equations are iteratively used until the lattice Green's function and self-energy converge to a desired accuracy. The output of the calculations is the momentum-independent converged Green's function $G(\omega)$ and self-energy $\Sigma(\omega)$ which contain all relevant system information. Therefore, for the first step of our work we focused mainly on the convergence of the Green's function and self-energy as a function of inverse temperature β, interaction strength U, mass-imbalance t_f, and chemical potential μ which

in half filling is equal to zero.

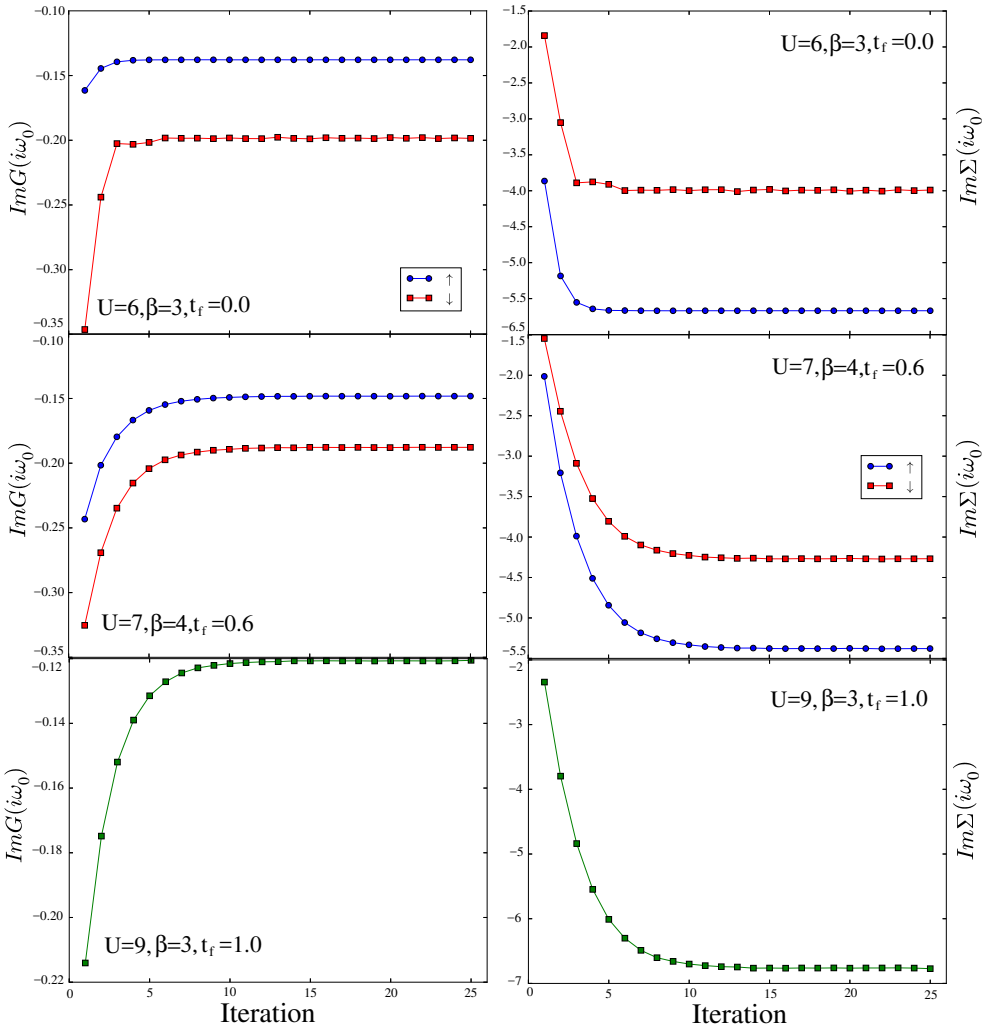

Figure 3.1 – Results as a function of DMFT iteration for: *left columns*, imaginary part of the Green's function; *right columns*, imaginary part of the self energy at given parameters. Data shown for $\mu = 0$.

The imaginary part of the Green's function and imaginary part of the self-energy at the first Matsubara frequency ($i\omega_0$) as a function of iteration order are shown in the left and right panels of Fig. 3.1, respectively. We show this iteration process at some exemplary U and β values for the HM, mass-imbalanced, and FKM cases. The upper two panels in

Fig. 3.1 show the iterations at the FKM where $t_f = 0$. The middle two panels in Fig. 3.1 show the iterations at mass-imbalanced case which in this example $t_f = 0.6$, and the lower two panels in in Fig. 3.1 show the iterations at the HM case where $t_f = 1$. We use the last iteration as converged Green's function and self-energy and perform our calculation based on them. Imaginary part of the Green's function and the self-energy at some parameters as an example are presented in Fig. 3.2.

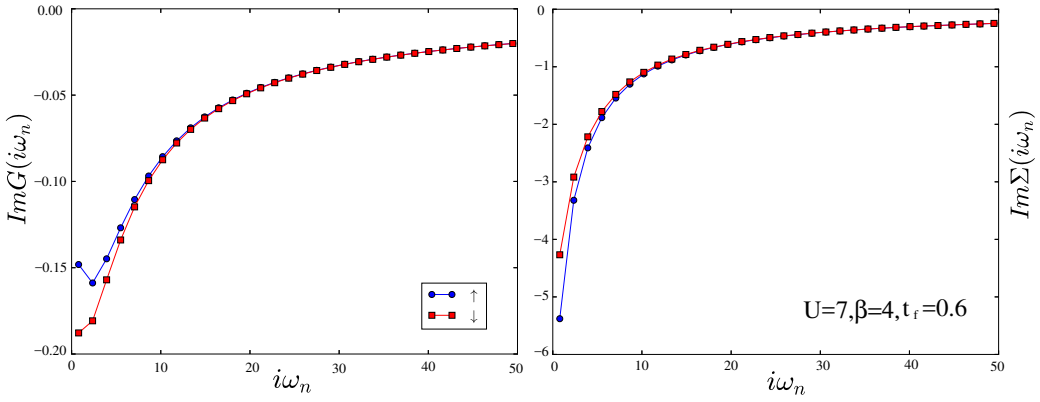

Figure 3.2 – Converged DMFT results for: *left*, imaginary part of the Green's function and *right*, the imaginary part of the self energy. Data is for $\mu = 0$.

3.2 Paramagnetic to Antiferromagnetic Transition Using DMFT

For the strong interactions and low temperatures, we observed the second-order paramagnetic (PM) to antiferromagnetic (AFM) transition also known as Néel ordering [66]. Near to the PM to AFM phase transition, the Green's function and the self-energy have the con-

vergence problem. Fig. 3.3 shows the iteration process of the imaginary part of the Green's function and imaginary part of the self-energy for exemplary U, β and t_f values. Here we only show the iterations for mass-imbalanced case of $t_f = 0.6$, 0.8. It seems the Green's function and the self-energy are about to converge, but at the end they do not. We used this as our first indication of second order phase transition.

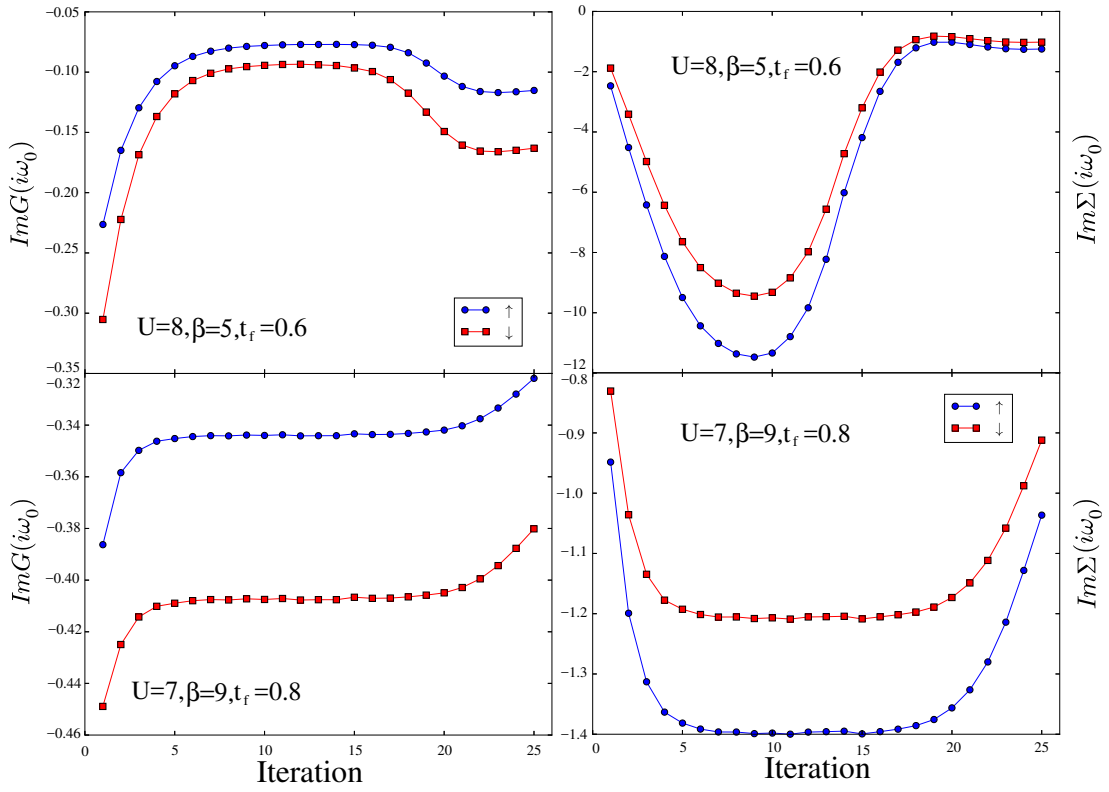

Figure 3.3 – Results as a function of DMFT iteration for: *left columns*, imaginary part of the Green's function, and *right columns*, imaginary part of the self-energy. Data for parameters which can not converge.

Fig. 3.4 shows the variation of S_z as a function of temperature T at some exemplary U and t_f values. S_z in the left panel of Fig. 3.4, at T=0.22 , which is marked by arrow, is

non-zero. Similarly, in the right panel of Fig. 3.4, at T=0.25, marked by arrow, $S_z \neq 0$. We use these points as onset of the AFM state.

Note that we are solving the DMFT with only one impurity site, and the assumption that the bath is paramagnetic. When $S_z \simeq < n_\uparrow - n_\downarrow > \neq 0$ this assumption breaks down and we refer to this boundary as the AFM state, since it is known from DCA studies.

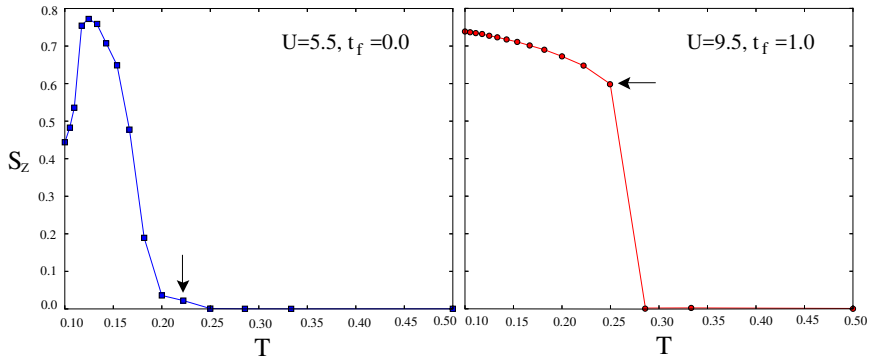

Figure 3.4 – S_z as a function of temperature: *left*, at T=0.222 ($\beta = 4.5$) and *right*, at T=0.25 ($\beta = 4.0$) are two points in which $S_z \neq 0$. Data is for $\mu = 0$ using DMFT.

The corresponding phase diagram obtained by DMFT for the square lattice is depicted in Fig. 3.5. The two points in Fig. 3.4 at which the system is in AFM state are marked by arrows in Fig. 3.5. We can conclude that the mass imbalance results in a relative increase of the critical temperature. The critical temperature in Néel ordering is called Néel temperature [1]. We obtain max$[T_c(t_f = 1)] \approx$0.28 and max$[T_c(t_f = 0)] \approx$0.33.

We would like to emphasize here that, as described in Sec. 2.1, based on the discussion in [32], for the mass-imbalanced case where $J_\parallel > J_\perp$, long range Z-antiferromagnetic order is permitted, and the Mermin-Wagner theorem [67], which prevents long-range order at

[1] Above this temperature, an antiferromagnetic material becomes paramagnetic.

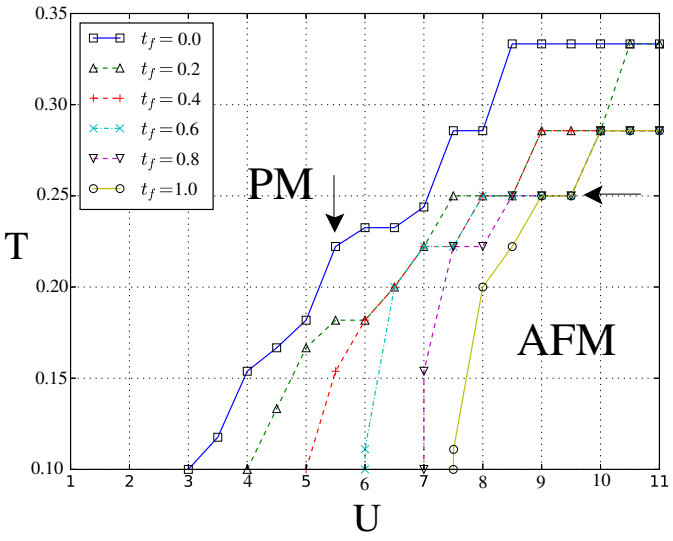

Figure 3.5 – Critical temperature for Néel ordering of the half filled Hubbard model at different values of the mass-imbalance parameter in a square lattice, obtained within DMFT.

finite temperature in low dimensions ($D \leq 2$), is applicable only to the rotation symmetry of the Hamiltonian (2.4) in the XY plane. Nonetheless, Mermin-Wagner theorem works only for infinite system size with continuous symmetries, and we believe since our system is finite, we capture the second order PM-AFM phase transition.

3.3 Fermi Liquid to Non-Fermi Liquid Crossover Using DMFT

The interaction-driven metal-to-insulator (MI) transition has been for many years one of the most interesting topics in the field of strongly-correlated electron systems. Understanding of the MI transition, particularly in the two-dimensional systems, has been challenging. In this section, we were also interested in investigating this MI transition; however, the

recent work [68] using Self-energy Determinantal Diagrammatic Monte Carlo and DCA (for infinite system size) methods has indicated that the low temperature crossover from the metallic Fermi liquid (FL) to the quasi-AFM insulator preempts and precludes the MI transition, and there is a state called non-Fermi liquid (nFL) between FM and quasi-AFM insulating states. Consequently, we aim to study the FL to nFL crossover in our system.

In order to proceed our investigation, we focus on PM state and study the destruction of the FL as a function of interaction, inverse temperature, and mass-imbalance. To obtain the FL-nFL crossover, we discriminate between FL and nFL solution by means of the imaginary part of the self-energy $\Sigma(i\omega_n)$. The FL and nFL solutions are characterized by a negative and positive slope for self-energy respectively, when $\omega_n \to 0$ [68]. We take this as the criterion for discriminating FL and nFL solutions. Fig. 3.6 shows this imaginary part of the self-energy for exemplary U values at $\beta = 4$ and mass-imbalance $t_f = 0.6$ in half-filling.

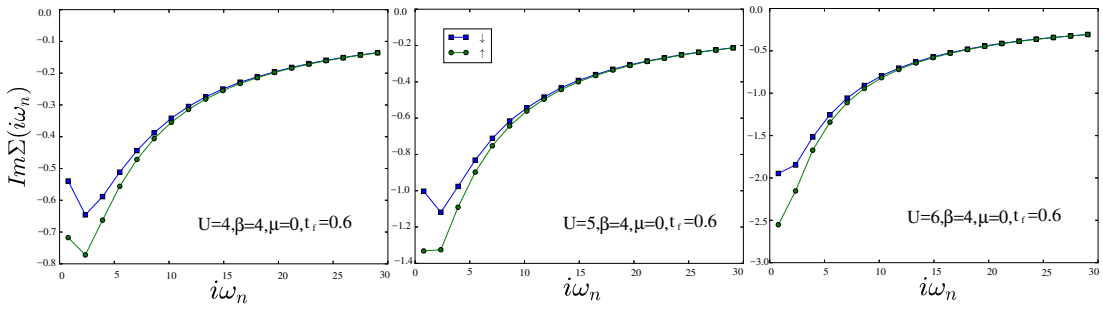

Figure 3.6 – Imaginary part of the self-energy at given parameters as an indicator for a FL and nFL solution obtained within DMFT. *left*: both spin-up and spin-down are in FL solution, *middle* spin-up in FL and spin-down in nFL solutions, and *right* both spin-up and spin-down are in nFL solution.

Considering above explanation, we use $\Delta\Sigma$ as our measure in the FL-nFL crossover

which is defined as:

$$\Delta\Sigma = Im\Sigma(i\omega_0) - Im\Sigma(i\omega_1) \tag{3.1}$$

If $\Delta\Sigma > 0$ the state is a metallic FL; when the reverse is true and $\Delta\Sigma < 0$, the state is nFL. We draw $\Delta\Sigma$ versus U, t_f and β and if $\Delta\Sigma$ changes its sign, it marks the crossover values which we denote with U^*, t_f^* and β^*. The crossover values are then used in obtaining the FL-nFL diagram. In the following we show how DMFT results produce the crossover values (U^*, t_f^*, β^*). All $\Delta\Sigma$ figures for different mass-imbalance t_f, inverse temperatures β, and interaction U are shown in Appendix B.

Fig. 3.7 shows how crossover interactions U^*, which are marked by a black circle, are obtained. This figure in general shows that by increasing the interaction, FL-nFL crossover happens. In Fig. 3.7 which is the variation of $\Delta\Sigma$ versus U, all $\Delta\Sigma$ are small towards $U \to 0$, and for intermediate values of U and β, $\Delta\Sigma$ is always positive which means the system is in the FL regime. For the large values of U, $\Delta\Sigma$ going to negative sides which shows the system crossing to nFL regime. At high temperature ($\beta = 2$), $\Delta\Sigma$ is negative which means the system is always in nFL regime. In addition, at lower temperature ($\beta > 5$) the system is magnetized and is in AFM state. Note that at $\beta = 5$, while for spin-up electrons FL-nFL crossover happens, for spin-down one, the system going to AFM state. Here we show the results only for $t_f = 0.8$. Data for other mass imbalance parameters can be found in Appendix B. Measured crossover interactions are presented in Table 3.1.

Fig. 3.8 ilustrates how the crossover mass-imbalance t_f^* is produced. Generally, Fig. 3.8 which is the variation of $\Delta\Sigma$ as a function of t_f, shows that by increasing the mass imbalance (decreasing the t_f) FL-nFL crossover happens. All $\Delta\Sigma$ for spin-up electrons are approaching almost same value towards $t_f \to 0$, and we have FL-nFL crossover for all

Table 3.1 – Crossover interactions U^* for spin-up and spin-down electrons at $t_f = 0.8$ and different values of inverse temperatures.

β	3	4	5
$U^*_\uparrow$	4.70	6.61	7.41
$U^*_\downarrow$	5.44	6.85	-

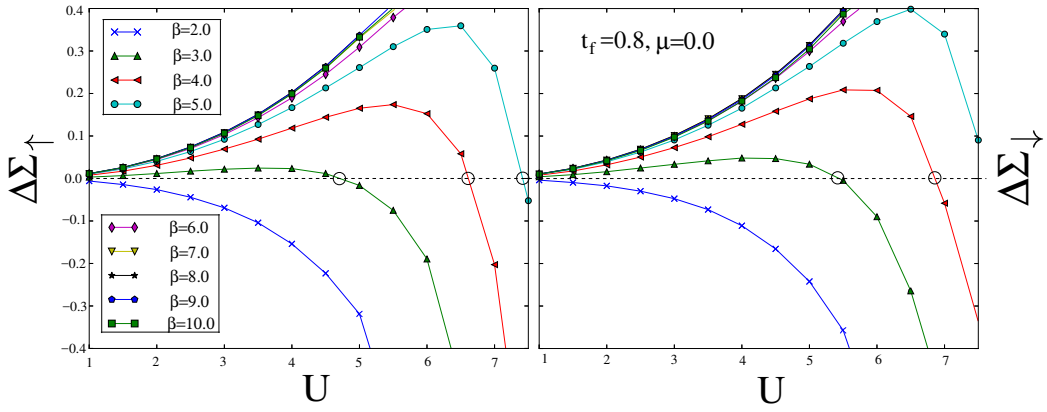

Figure 3.7 – DMFT results for $\Delta\Sigma$ as a function of interaction U at different inverse temperatures β and mass-imbalance $t_f = 0.8$. *left*: is for spin-up, and *right*: is for spin-down.

values of β. However, for spin-down electrons, we see the different behavior and FL-nFL crossover exist only for $\beta = 3$, 4 and 5. For spin-down electrons and at lower temperature, the system is always in FL regime. Here we only show the results for U=3. Data for other interaction values can be found in Appendix B. Measured crossover mass imbalance are presented in Table 3.2.

Finally, in Fig. 3.9 we show how DMFT results produce crossover inverse temperatures β^*. Fig. 3.9, which is the variation of $\Delta\Sigma$ as a function of β, shows that by increasing the temperature FL-nFL crossover happens. At $t_f = 0$, $\Delta\Sigma$ for spin-up electrons are always

Table 3.2 – Crossover mass imbalance parameters t_f^* for spin-up and spin-down electrons at U=3 and different values of inverse temperatures.

β	3	4	5	6	7	8	9	10
$t_{f\uparrow}^*$	0.69	0.47	0.35	0.28	0.23	0.19	0.17	0.16
$t_{f\downarrow}^*$	0.49	0.22	0.08	-	-	-	-	-

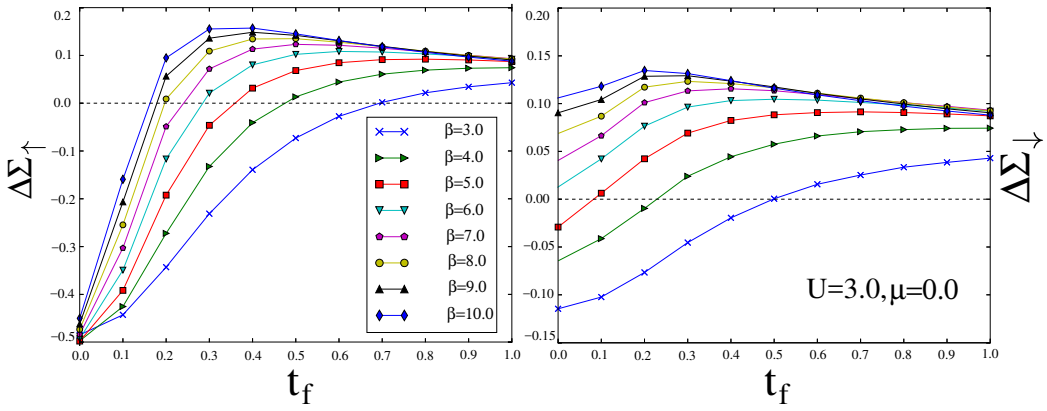

Figure 3.8 – DMFT results for $\Delta\Sigma$ as a function of mass-imbalance t_f at different inverse temperatures β and interaction U = 3.0. *left*: is for spin-up, and *right*: is for spin-down.

negative which means the system is always in nFL regime. However, for spin-down electrons, FL-nFL crossover exists for all values of mass-imbalance parameters. Here we only show the results for U=2. Data for other interaction values U can be found in Appendix B. Measured crossover inverse temperatures are presented in Table 3.3.

Using the crossover values from $\Delta\Sigma$ figures (3.7, 3.8 and 3.9), crossover diagrams , Fig. 3.10, Fig. 3.11 and Fig. 3.12 are obtained. Fig. 3.10 is a spin dependent FL-nFL crossover as a function of interaction strength U and mass imbalance parameter t_f in which the FL regime is destroyed not only by increasing the interaction, but also by increasing the

Table 3.3 – Crossover inverse temperatures β^* for spin-up and spin-down electrons at U=2 and different values of mass imbalance parameters.

t_f	1.0	0.8	0.6	0.4	0.2	0.0
$\beta^*_\uparrow$	2.32	2.68	3.21	4.25	7.08	-
$\beta^*_\downarrow$	2.32	2.51	2.74	3.06	3.74	4.60

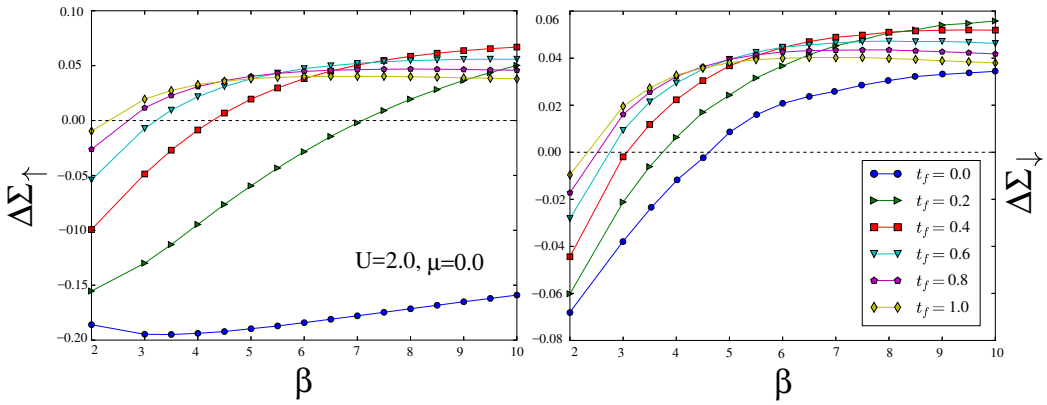

Figure 3.9 – DMFT results for $\Delta\Sigma$ as a function of inverse temperatures β at different mass-imbalance t_f and interaction U = 2.0. *left*: is for spin-up, and *right*: is for spin-down.

mass-imbalance. As we see in Fig. 3.10 for example at $\beta = 5$, the strength of the crossover interaction for both spin-up and spin-down, $U^*_\uparrow$ and $U^*_\downarrow$, decreases monotonically as the mass imbalance grows (t_f decreases) so that the minimum $U^*_\downarrow$ is realized when one of the species is localized where we reach the FKM limit ($t_f = 0$). By increasing β (lowering the temperature) the AFM state emerges which suppresses the PM states including FL/nFL regimes. As we go to lower temperatures the nFL regime shrinks so that this regime is completely collapsed for spin-down at $\beta = 9$. At $\beta = 10$, a small part of the nFL regime survives only for spin-up. Upon decreasing the temperature, AFM state is increasing; con-

sequently, we expect that at $\beta \to \infty$ the AFM state would be the dominant state in any U interaction.

Fig. 3.11 is also a spin dependent FL-nFL crossover as a function of inverse temperature β and mass imbalance t_f in which the FL(nFL) regime is increasing (decreasing) by increasing β.The crossover inverse temperature for spin-up and spin-down, $\beta^*_\uparrow$ and $\beta^*_\downarrow$, increases monotonically as the mass imbalance increases or t_f decreases. As we see in Fig. 3.11 at U=1, 2 and 3, the maximum $\beta^*_\downarrow$ is obtained when we are in the FKM limit where $t_f = 0$. In Fig. 3.11 at U=4 and low temperatures, the AFM emerges which is expected here also at zero temperature, the AFM would be the dominant state in our system.

As in the Hubbard case ($t_f = 1$), the Fermi-liquid state seen in the mass-imbalanced HM exists below a certain coherence temperature T_{coh}[2]. Above T_{coh}, the thermal disorder is too strong for the quasiparticles to survive and the good metallic FL behavior is gradually lost. Let us here mention that we use $\Delta\Sigma$ in determining the coherence temperature. Thus, coherence temperatures are the temperatures at which FL-nFL crossover happens. Our results for T_{coh}, obtained within DMFT, are plotted in Fig. 3.12. As we see, T_{coh} is decreasing by increasing interaction and mass imbalance so that this decrease is faster to spin-up electrons. As one increases the temperature above T_{coh}, the solution has a rapid crossover toward a new bad metallic state, i.e., the nFL state. We obtained T_{coh} for the HM case, $0.25 \leq T_{coh}(t_f = 1) \leq 0.43$ and for the FKM case, $0.11 \leq T_{coh(\downarrow)}(t_f = 0) \leq 0.22$. Note that $T_{coh(\uparrow)}$ is vanished for the FKM which means at $t_f = 0$, spin-up electrons are in nFL regime.

The phase diagram of the half-filled mass imbalanced Hubbard model at different mass-

[2]The T_{coh}, experimentally, is characterized by a specific heat that has linear dependence to temperature [15].

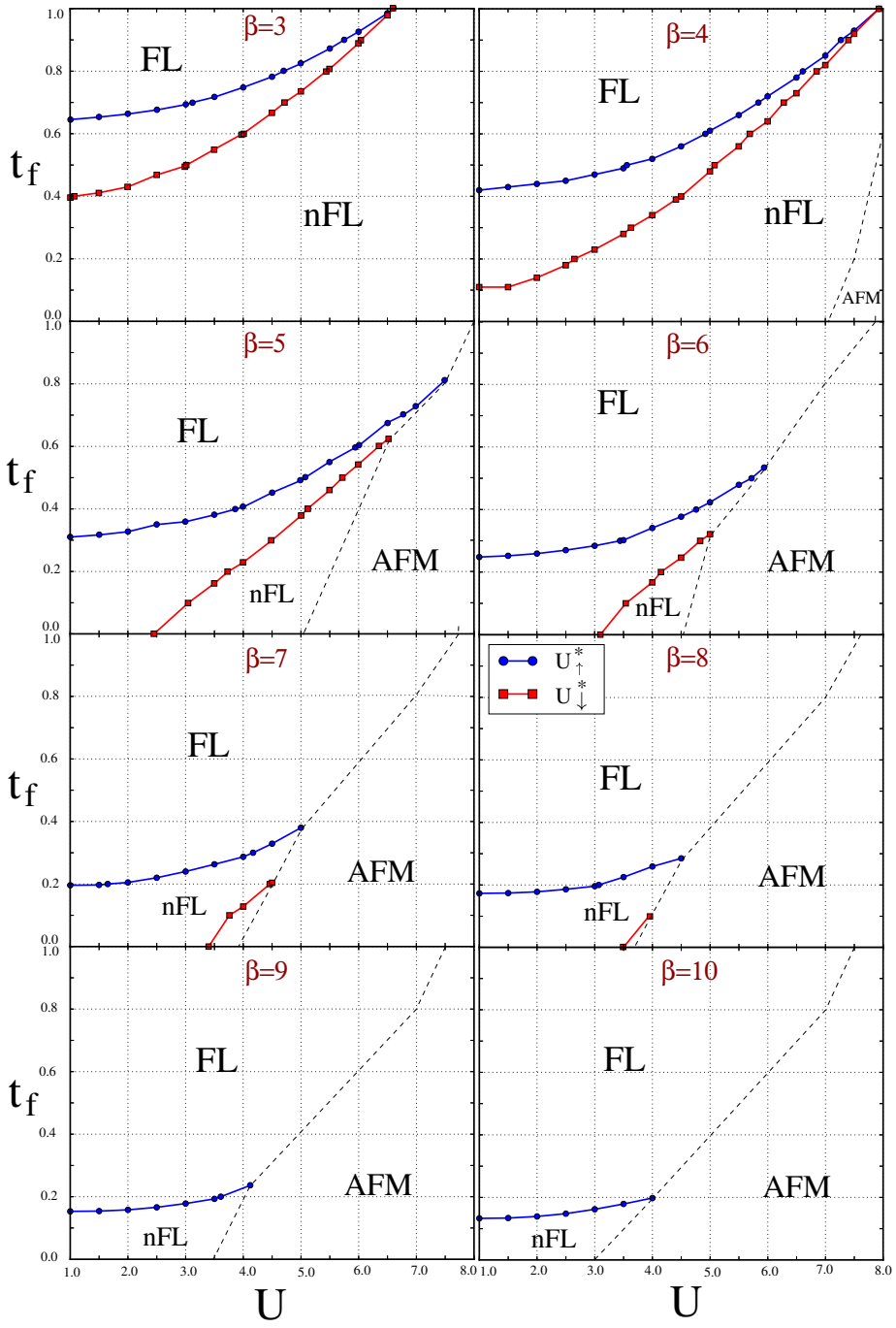

Figure 3.10 – Crossover diagram of the FL/nFL/AFM states as a function of interaction strength U and mass-imbalance t_f at $\beta = 3,4,5,6,7,8,9,10$ and $\mu = 0$ obtained within DMFT.

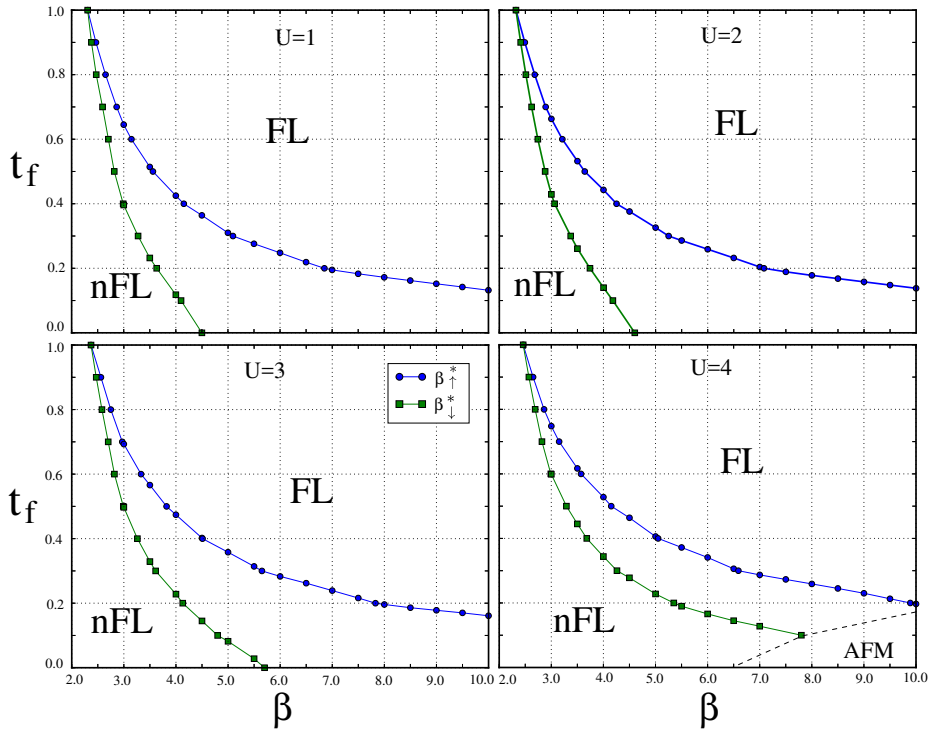

Figure 3.11 – Crossover diagram of the FL to nFL as a function of inverse temperature β and mass-imbalance t_f at U = 1, 2, 3, 4 and $\mu = 0$ obtained within DMFT.

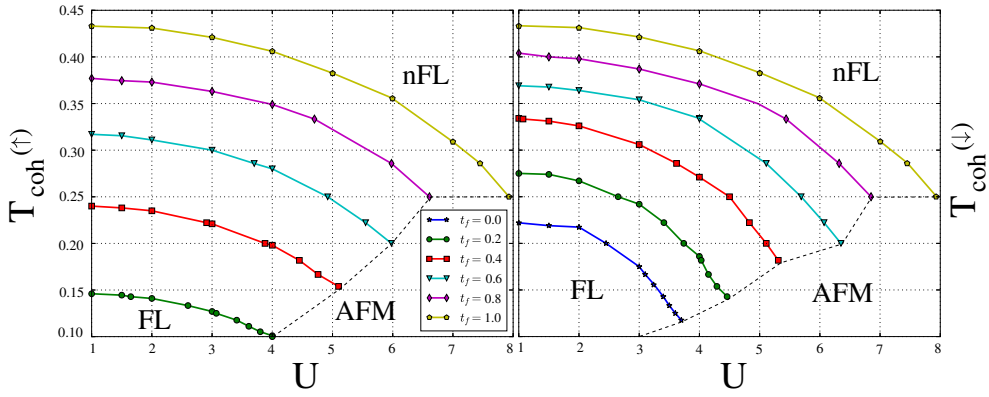

Figure 3.12 – Crossover diagram of the FL to nFL which shows the behavior of T_{coh} as a function of interaction U for various values of the mass-imbalance factor t_f. The data is in half-filling $\mu = 0$ obtained within DMFT.

imbalance t_f and temperature $0.5 \leq T \leq 0.1$ is depicted in Fig. 3.13. Brown areas show the FL state for both spin-up and spin-down electrons, and white areas show only FL state for spin-down electrons. At temperature $T \leq 0.33$, we observe the AFM state whose domain increases as mass-imbalance increases (t_f decreases). At temperatures $0.11 \lessapprox T \lessapprox 0.28$ there is a FL-nFL-AFM transition which is different for spin-up and spin-down electrons. At sufficiently low temperature (T=0.1), we do not observe the nFL regime and there is a direct FL to AFM transition. Note that the $FL_{\downarrow}$, which is included in the white and brown areas, is always bigger than $FL_{\uparrow}$, which is only brown area. As the mass-imbalance grows and we approach the FKM ($t_f = 0$), the $FL_{\uparrow}$ decreases and is completely lost at $t_f = 0$. This means that spin-up electrons are more affected by the interactions.

3.4 Spectral Function

In the previous section we have plotted a phase diagram in the imbalance-correlation plane which highlights how the FL/nFL states turn into an AFM. We now extend our analysis to the spectral functions, which is a key quantity to characterize the nature of the metallic states and the approach to the insulating state. Most interestingly, spectral functions are experimentally accessible through trapped cold atomic systems, radio spectroscopy or Raman spectroscopy.

Since for lower temperatures the AFM is dominant state, we prefer to do the analysis for $\beta = 6.5$ and interaction strength U = 4 which is considered as strong-coupling regime. As shown in Fig. 3.11 for U=4 at $\beta = 6.5$, it is below the AFM transition point for any value of t_f. Therefore we will always be in a PM state, even if decreasing t_f will drive the system close to an AFM transition. In order to investigate how the effect of correlations

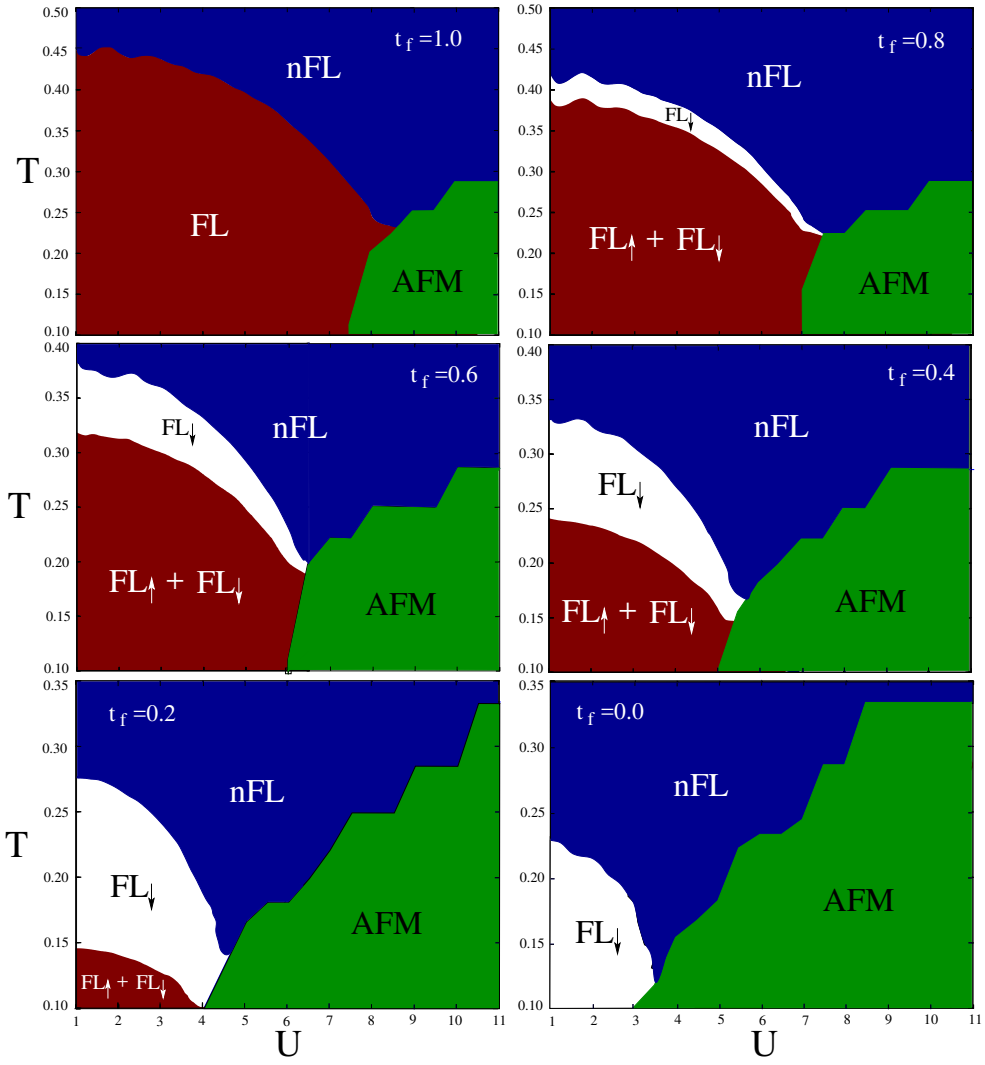

Figure 3.13 – Phase diagram of the half-filled 2D mass-imbalanced Hubbard model as a function of interaction U and temperature T at mass-imbalance t_f=1.0, 0.8, 0.6, 0.4, 0.2, 0.0, obtained by DMFT.

increases when t_f gets smaller, we choose t_f from balanced one to very large imbalance. Fig. 3.14 presents the spectral densities of the spin-up electrons and spin-down electrons for different values of the mass imbalance $t_f = 0.0, 0.4, 0.8, 1.0$. For U = 4, as representation of large values of U, the behavior of these spectral functions strongly depends on the mass imbalance t_f. The evolution of the electron spin species as a function of t_f at $\omega = 0$ show the

crossover from the FL with central quasiparticle peak to the nFL without the quasiparticle peak, even if the driving parameter is not the interaction. At high energy $\omega \sim$ 2U, the physics of both electron species is dominated by the interaction that induces the formation of Hubbard bands with incoherent excitations around $\omega = \pm U$[3]. As we see in Fig. 3.14, the spectral densities of spin-down electrons at $\omega = 0$, which shows the density at the Fermi level, are always bigger than for spin-up electrons at any values of mass-imbalance.

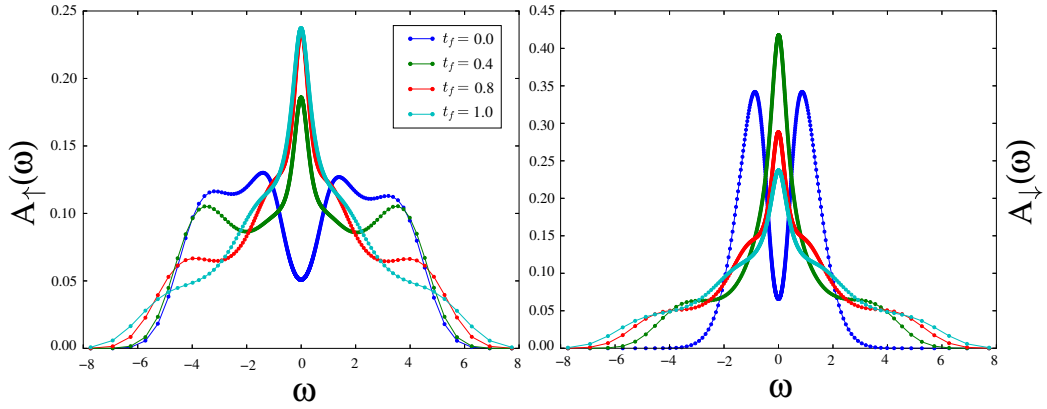

Figure 3.14 – Spectral functions of the *left* spin-up and *right* spin-down for U = 4, $\mu = 0$, β=6.5 and t_f= 0.0, 0.4, 0.8, 1.0.

We now focus our analysis on the spectral density at $\omega = 0$ which is denoted by A(0). Fig. 3.15 shows the A(0) as a function of mass-imbalance t_f at different temperatures and interaction strengths. We are, in fact, moving along a vertical line pointing toward the FL to nFL transition at $\beta = 5, 7, 10$ and specified U values in the crossover diagram of Fig. 3.10. Considering the spin-up, when we are crossing from the nFL regime to the FL regime, the A(0) is increasing, monotonically, for any t_f values and temperatures, even if the increase

[3] At typical Mott-Hubbard metal-insulator transition, the separated Hubbard bands are formed at $\omega = \pm U/2$.

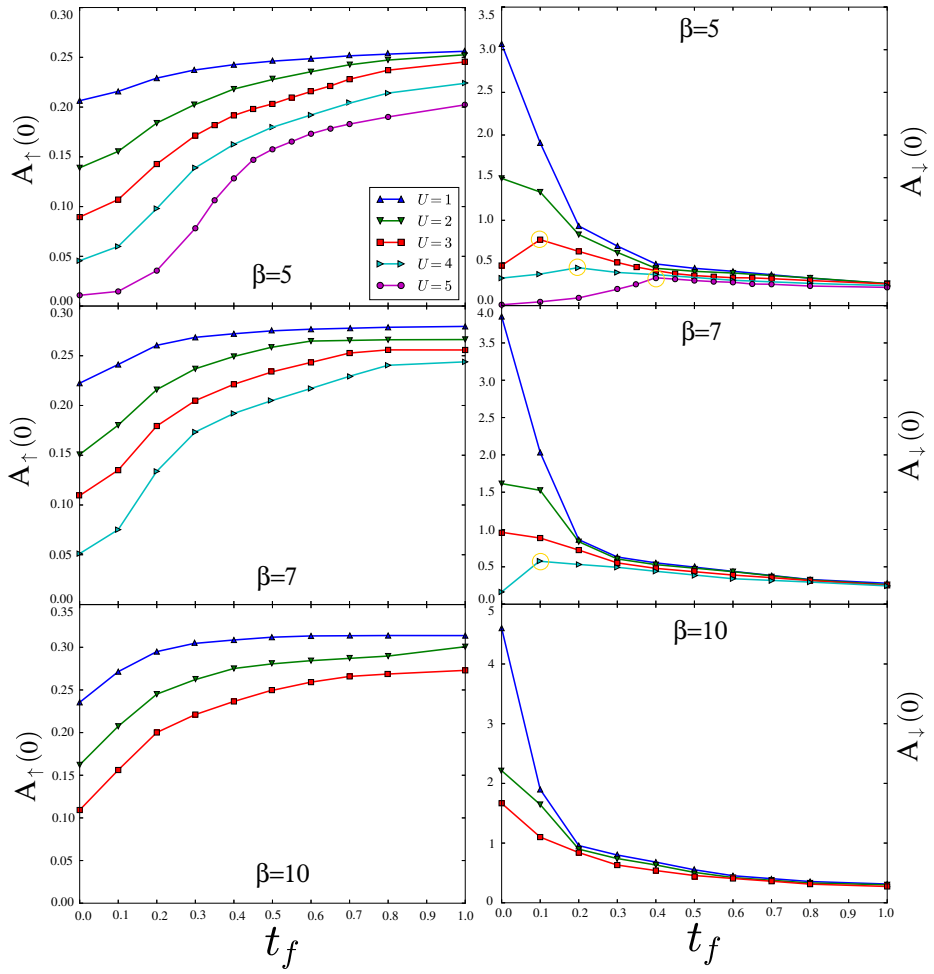

Figure 3.15 – Spectral densities at $\omega = 0$ as a function of t_f of the *left* spin-up and *right* spin-down at $\beta = 5, 7, 10$, $\mu = 0$, and different interaction strength.

is much more pronounced for large interactions. However, most interestingly, this trend is quite different for spin-down electrons. As we see at $\beta = 5$, for U=1, and 2, the system is in the FL regime and the A(0) is decreasing by increasing the t_f; nonetheless, for U=3, 4, and 5, the A(0), corresponding to the nFL in the crossover diagram (Fig. 3.10), initially increases and reaches its highest values (highlighted with the yellow circle) in the FL-nFL crossover, and then starts to decrease in the FL regime. We see the same trend for $\beta = 7$ in

which at U=1, 2, and 3, the A(0) in the FL regime decreases by increasing the t_f, but for U=4 follows the same trend as we had for $\beta = 5$ at U=3, 4 and 5. For $\beta = 10$, the system is always in the FL at any t_f so that the A(0) decreases as t_f increases.

3.5 Mass Renormalization

In this section we investigate the main effect of interaction measured by the effective (or renormalized) mass m^*. To do so we use Eq. (2.21) and plot variation of quasiparticle weight Z as a function of interaction U. The left panel in Fig. 3.16 shows the Z of both species for three different mass imbalance factors t_f = 0.4, 0.8, 1.0. We choose the intermediate temperature $\beta = 4$ which is above the minimum coherence temperature for any t_f values to see the FL/nFL crossover without entering the AFM state. At all three t_f values the quasiparticle weight is decreasing as interaction increases which means that FL-nFL crossover can happen. For the $t_f = 1.0$, Z is bigger and is almost linear in interaction which shows that in the HM case the electrons are less affected by the interactions compared to the mass-imbalanced HM where $t_f \neq 1$. For the imbalance t_f= 0.8 and 0.4, spin-up (light) electrons have a smaller Z ($Z_\uparrow < Z_\downarrow$) which means they are more renormalized compared to their spin-down (heavy) partners, even if the effect is much more pronounced for t_f = 0.4. These results show that the spin-up (light) species with smaller bare mass are more affected by correlations than the spin-down (heavy) ones. Our solution actually shows that when two species with different mobilities are mixed, the interactions tend to balance their properties.

The right panel in Fig. 3.16 shows the variation of $\Delta Z \equiv Z_\downarrow - Z_\uparrow$ as a function of U. For weak and intermediate interaction strengths ($1 \leq U \leq 4$) the maximum difference between

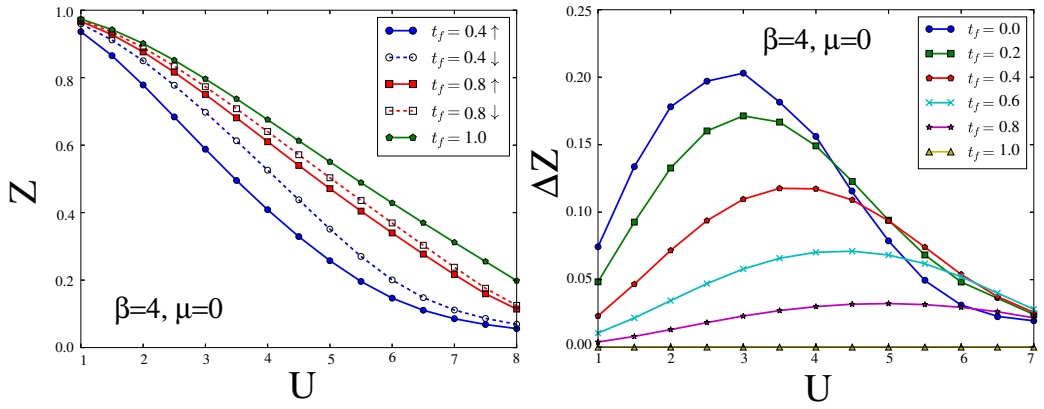

Figure 3.16 – DMFT results of *left*: quasiparticle weight Z, *right*: ΔZ as a function of the interaction strength U at $\beta = 4$, $\mu = 0$, for various values of the mass-imbalance factor t_f.

spin-down quasiparticles and spin-up quasiparticles happens at $t_f = 0$. However, this trend changes for strong interaction strengthss (U$\geq$ 4). For U = 5 the maximum ΔZ is at $t_f = 0.2$, for U = 6, 7, the maximum ΔZ is at $t_f = 0.4$, and for U = 7 the maximum ΔZ happens at $t_f = 0.6$.

3.6 Double Occupation

We compute the double occupation $\langle n_\uparrow n_\downarrow \rangle$, another physical observable accessible in cold atom system which can be used to establish a link between the model and the experiments. The results are shown in Fig. 3.17 for various values of U and t_f at finite temperature $\beta = 4$. We observe a lower double occupation in the nFL regime which implies that most probably each site is almost singly occupied. In contrast, when one approaches the metallic FL state upon decreasing U, the higher kinetic energy and lower potential energy together lead to a strong increase in the number of doubly occupied sites. At smaller values of t_f there is a sharper transition from the metallic FL to nFL state. The metallic FL state is

characterized by linear decrease of the double occupation with increasing interaction U. However, in the FL-nFL crossover points (marked with arrows in the inset of Fig. 3.17), the linear dependence is lost, and at larger values of the interaction, the double occupation remains low and weakly U-dependent. At smaller values of t_f, when the system is more imbalanced, due to the reduced values of the crossover interaction U^*, there is a sharper crossover from the metallic FL to nFL state. However, at large values of t_f, when the system is less imbalanced, because of the larger U^*, thus we observe a rather slow FL-nFL crossover.

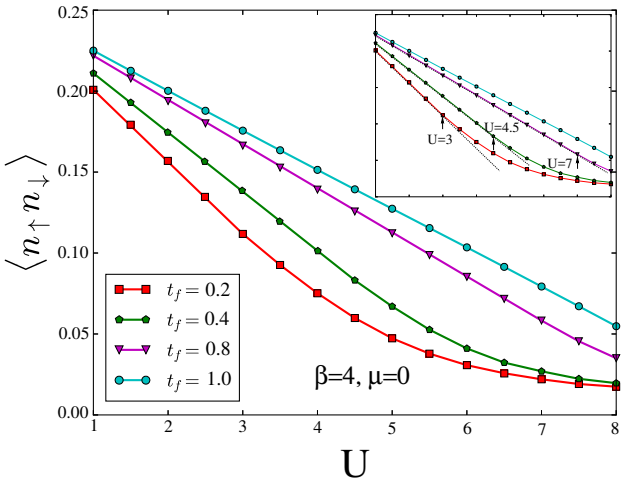

Figure 3.17 – DMFT results of double occupancy as a function of U at $\beta = 4$, $\mu = 0$, for different values of t_f. The inset shows the spin-down crossover interactions $U^*_\downarrow$ where both spin species are in nFL state.

3.7 Fermi Liquid to Non-Fermi Liquid Crossover Using DCA

As discussed earlier, in order to have an exact results, we use the DCA in which we increase the number of cluster N. However, computational cost, which scales with N^3 and β^3, makes it hard to solve problem with large scale clusters. Therefore, in this section we investigate the FL-nFL crossover with small-scale cluster (8-site and 16-site) at only one temperature ($\beta = 4$).

As described in Sec. 2.2.4, DCA is an extension of the DMFT in which the nonlocal dynamical correlation is also considered. Therefore, the Green's function and the self-energy as main output of our calculations, are momentum-dependent. Here, we start with an 8-site cluster and then expand the cluster to 16-site. In the 8-site cluster, the eight k points on the Fermi surface (FS) are: $k_1 = (\pi/2, \pi/2)$, $k_2 = (-\pi/2, -\pi/2)$, $k_3 = (0,0)$, $k_4 = (\pi, \pi)$, $k_5 = (-\pi/2, \pi/2)$, $k_6 = (\pi/2, -\pi/2)$, $k_7 = (0, \pi)$, and $k_8 = (\pi, 0)$.

Our main result is summarised in Fig. 3.18 which shows the FL-nFL crossover of the half-filled mass-imbalanced Hubbard model as a function of interaction strength U and mass imbalance t_f at $\beta = 4$. The left panel of Fig. 3.18 shows the 8-site DCA result and the right panel of the Fig. 3.18 shows the 8-site DCA and DMFT results to have a better comparison between two methods. In generating this crossover diagram we take the average of the self-energy at the aforementioned eight k points to produce the localized self-enegy, and then we use $\Delta\Sigma$ to obtain the crossover values as we had in the DMFT method. As we see in the right panel on Fig. 3.18, for the large values of the interaction, the crossover interactions for both spin-up and spin-down, $U^*_\uparrow$, $U^*_\downarrow$, are reduced in 8-site cluster DCA. In contrast, for the weak values of the interaction, the crossover interactions

$U^*_\uparrow$, $U^*_\downarrow$, are almost the same for both methods.

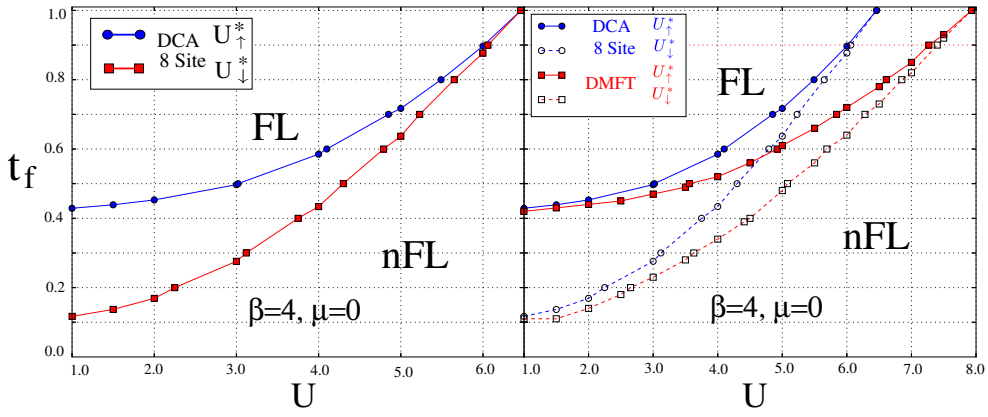

Figure 3.18 – FL-nFL crossover diagram as a function of interaction strength U and mass imbalance t_f at $\beta = 4$, $\mu = 0$ obtained within *left*: localized 8-site DCA, *right*: localized 8-site DCA and DMFT.

The left panel of Fig. 3.19 shows the same FL-nFL crossover using 8-site cluster DCA at the anti-nodal point $k_{an} = (\pi, 0)$ and the nodal point $k_n = (\pi/2, \pi/2)$. The FL-nFL crossover first appears at the anti-nodal point and then at the nodal point. Most interestingly, as we see in the right panel of Fig. 3.19, the crossover for nodal point and the localized 8-site DCA almost coincide with each other with a little deviation at large values of t_f.

In order to increase our results' accuracy and obtain the exact results, we increase the cluster size and do our analysis to 16-site cluster. The left panel of Fig. 3.20 shows the FL-nFL crossover as a function of interaction strength U and mass imbalance parameter t_f using 16-site cluster DCA. In order to have a good comparison between 16-site and 8-site cluster DCA with DMFT results, we draw them in same frame (see right panel of Fig. 3.20). By increasing the cluster size, the crossover interaction U^* is reduced which this reduction is more at large values of the interaction. At weak interaction, $t^*_{f\uparrow}$ in 16-site DCA deviates from 8-site DCA and DMFT. However, $t^*_{f\downarrow}$ is almost the same with 8-site DCA and

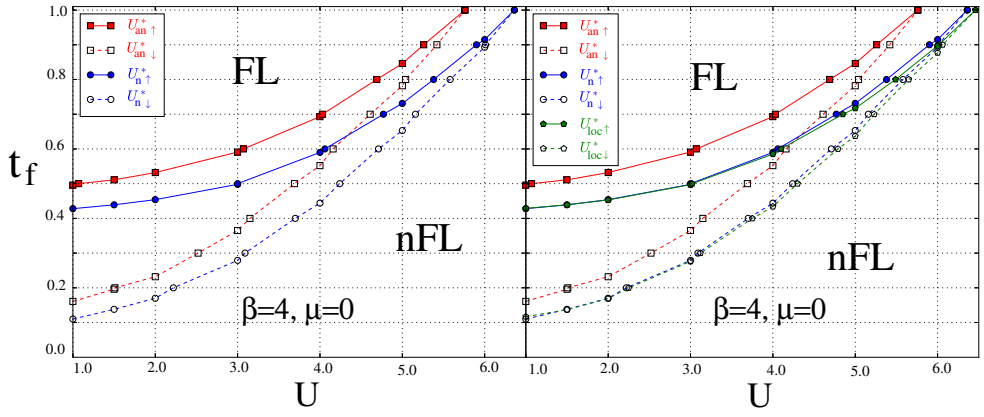

Figure 3.19 – FL-nFL crossover diagram as a function of interaction strength U and mass imbalance t_f at $\beta = 4$, $\mu = 0$ obtained within *left*: 8-site DCA at $k_{an} = (\pi, 0)$ and $k_n = (\pi/2, \pi/2)$, *right*: 8-site DCA at $k_{an} = (\pi, 0)$, $k_n = (\pi/2, \pi/2)$, and localized 8-site DCA.

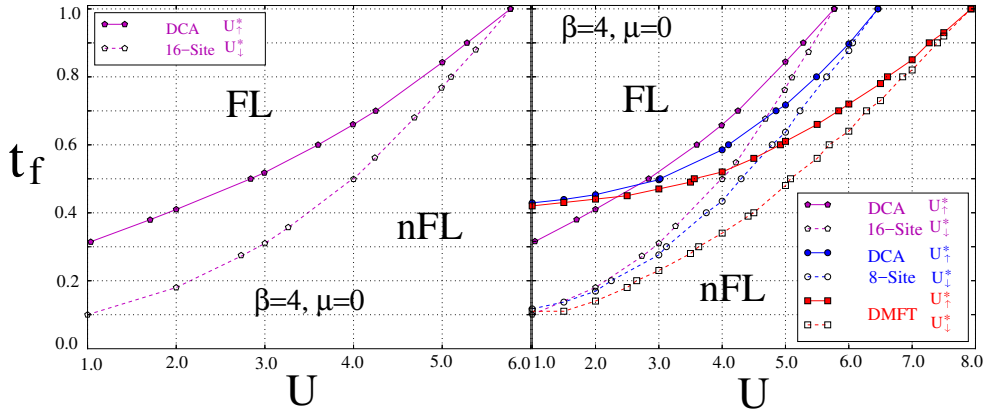

Figure 3.20 – FL-nFL crossover diagram as a function of interaction strength U and mass imbalance t_f at $\beta = 4$, $\mu = 0$ obtained within *left*: localized 16-site DCA, *right*: localized 16-site, 8-site DCA and DMFT.

DMFT results. Note that at large values of the interaction, the difference between DMFT and 8-site DCA is more than the difference between the 16-site and 8-site DCA. Thus, we believe this difference is not getting much bigger for large scale cluster size.

Chapter 4

Discussion and Conclusion

We have analyzed the half-filled mass-imbalanced Hubbard model on a 2D square lattice at finite temperature. In the first part of the thesis, we investigated the PM-AFM transition by the DMFT. Our phase diagram, Fig. 3.5, at large values of interaction strength and low temperatures, shows a second order phase transition, i.e. Néel ordering, at all values of mass imbalance. Critical Néel temperature increases with the mass imbalance which is in good agreement with the DMFT study of mass-imbalanced ultracold atoms in optical lattice [32]. As we go to lower temperatures and increase the mass imbalance, the AFM is the dominant state so that we expect the ground state of the mass-imbalanced Hubbard model like that of the balanced Hubbard model on the square lattice at half filling to be the AFM state for any on-site interaction.

In the second part of the thesis, as our most important part in terms of effort and time spent, we analyzed the FL-nFL crossover of the model within the paramagnetic phase by DMFT and small cluster DCA methods. Our main result is summarised in Fig. 3.13 which shows the spin dependent metallic FL to nFL state including Néel ordering for different

values of the mass imbalance t_f. Above certain coherence temperature, due to the strong thermal disorder, the quasiparticles can not survive; therefore, the metallic FL behavior is lost and we enter the nFL state. This good-metal behavior is dependent on two other factor as well: the interaction strength U and the mass imbalance parameter t_f. We conclude that the FL to nFL crossover happens not only by increasing the interaction, but also by increasing the mass imbalance. The metallic FL for spin-up electrons is gradually lost as the mass imbalance increases so that at the FKM limit where $t_f = 0$, most interestingly, the FL for spin-up electrons (light electrons) is completely lost. This means that spin-up (light) electrons are more affected by the interaction than their spin-down (heavy) partners.

The behaviour of the spectral densities is strongly dependent on the mass imbalance t_f, and the spectral density of spin-down (heavy) electrons at $\omega = 0$, denoted by A(0), are always bigger than spin-up electrons at any values of the mass imbalance (Fig. 3.14). The variation of A(0) is completely different for spin-up and spin-down electrons. For the spin-up electron, A(0) increases, monotonically, while we are crossing from nFL to FL regime; however, for the spin-down, we observed a small peaks for A(0) at the nFL to FL crossover points (Fig. 3.15).

The variation of quasiparticle weight with interaction for both spin species shows us that the spin-up electrons (light species) is more renormalized than the spin-down (heavy) one, which implies spin-up (light) electrons is more affected by interaction than the spin-down (heavy) one. This is in good agreement with the results of [15, 31]. The important discussion about this behaviour is that in the case of two bands in a solid, both bands filled with up and down electrons, it is natural that the heavy-electron band with smaller hopping t is more affected and more renormalized by the interaction than the light-electron band. This increases the possibility of the orbital-selective Mott transition in which the more renormal-

ized heavy-band hopping approaches zero, while the light one remains metallic [31]. But in our case another effect competes with this universally expectation about the behavior of the renormalization factors. When the system is at half-filling and the correlation is strong enough, there is essentially one electron on each lattice site. In this situation, based on Pauli principle, if the light electron attempts to move, it has to move to a site which is already populated by a heavy one and the heavy one has to move to a site previously occupied by the light electron. This means that, if the light electrons attempt to move, the heavy ones are forced to move as well. When we are in this regime, we expect the renormalization factors Z to compensate the hopping imbalance. In other words we expect $Z_{light} < Z_{heavy}$, and this is what we observed in the left panel of Fig. 3.16.

When the system is in the FL regime, because of the higher kinetic energy and lower potential energy, the double occupation is more likely. In contrast, when we are moving to the nFL regime by increasing the interaction, since the double occupancy is decreasing, we believe that a big portion of the sites are singly occupied. When we increase the mass imbalance, the double occupancy is decreasing sharply. We also observed a small change in the slope of the linear decrease of the double occupancy at the FL-nFL crossover points.

We have shown the dependence of the crossover value of the interaction U^* for the FL-nFL crossover on the mass imbalance t_f via DMFT (Fig. 3.10) and small cluster DCA (Fig. 3.18 and Fig. 3.20) methods. In both methods, the crossover interaction U^* decreases as the mass imbalance grows. DCA reduces the U^* so that this reduction is the highest at large values of the interaction. At weak values of the interaction, for 8-site cluster, two methods almost coincide with each other; however, for 16-site cluster, this trend deviates for spin-up electrons and $t^*_{f\uparrow}$ is smaller than 8-site cluster and single-site DMFT results. For 8-site cluster, we investigate the FL-nFL crossover at the anti-nodal point $k_{an} = (\pi, 0)$ and

nodal point $k_n = (\pi/2, \pi/2)$ which are two important k points on the FS. Fig. 3.19 shows that the FL-nFL crossover happens at the anti-nodal point $k_{an} = (\pi, 0)$ earlier than at the nodal point $k_n = (\pi/2, \pi/2)$. Most interestingly, the crossover at the nodal point coincides with the localized DCA result which implies the nodal point is the most important point at the FL-nFL crossover.

Bibliography

[1] Vladan Celebonovic. The Hubbard model: Basic notions and selected applications. *Journal of Optoelectronics and Advanced Materials*, 11, 02 2010.

[2] Martin C. Gutzwiller. Effect of Correlation on the Ferromagnetism of Transition Metals. *Phys. Rev. Lett.*, 10:159–162, Mar 1963.

[3] Junjiro Kanamori. Electron Correlation and Ferromagnetism of Transition Metals. *Progress of Theoretical Physics*, 30(3):275–289, 09 1963.

[4] J. Hubbard and Brian Hilton Flowers. Electron correlations in narrow energy bands. *Proceedings of the Royal Society of London. Series A. Mathematical and Physical Sciences*, 276(1365):238–257, 1963.

[5] J. Hubbard and Brian Hilton Flowers. Electron correlations in narrow energy bands III. An improved solution. *Proceedings of the Royal Society of London. Series A. Mathematical and Physical Sciences*, 281(1386):401–419, 1964.

[6] N. F. MOTT. Metal-Insulator Transition. *Rev. Mod. Phys.*, 40:677–683, Oct 1968.

[7] Editorial. The Hubbard model at half a century. *Nature Physics*, 9:523, Sep 2013.

[8] Elliott H. Lieb and F. Y. Wu. Absence of Mott Transition in an Exact Solution of the Short-Range, One-Band Model in One Dimension. *Phys. Rev. Lett.*, 20:1445–1448, Jun 1968.

[9] Elliott Lieb and Daniel Mattis. Theory of Ferromagnetism and the Ordering of Electronic Energy Levels. *Phys. Rev.*, 125:164–172, Jan 1962.

[10] A.M.C. Souza, C.A. Macedo, and M.L. Moreira. Thermodynamics of the one-dimensional Hubbard model with next-nearest-neighbor hopping. *Physica B: Condensed Matter*, 354(1):293 – 296, 2004.

[11] J. P. F. LeBlanc, Andrey E. Antipov, Federico Becca, Ireneusz W. Bulik, Garnet Kin-Lic Chan, Chia-Min Chung, Youjin Deng, Michel Ferrero, Thomas M. Henderson, Carlos A. Jiménez-Hoyos, E. Kozik, Xuan-Wen Liu, Andrew J. Millis, N. V. Prokof'ev, Mingpu Qin, Gustavo E. Scuseria, Hao Shi, B. V. Svistunov, Luca F. Tocchio, I. S. Tupitsyn, Steven R. White, Shiwei Zhang, Bo-Xiao Zheng, Zhenyue Zhu, and Emanuel Gull. Solutions of the Two-Dimensional Hubbard Model: Benchmarks and Results from a Wide Range of Numerical Algorithms. *Phys. Rev. X*, 5:041041, Dec 2015.

[12] L. M. Falicov and J. C. Kimball. Simple Model for Semiconductor-Metal Transitions: SmB_6 and Transition-Metal Oxides. *Phys. Rev. Lett.*, 22:997–999, May 1969.

[13] Tom Kennedy and Elliott H. Lieb. An itinerant electron model with crystalline or magnetic long range order. *Physica A: Statistical Mechanics and its Applications*, 138(1):320–358, 1986.

[14] P Lemberger. Segregation in the Falicov-Kimball model. *Journal of Physics A: Mathematical and General*, 25(4):715–733, feb 1992.

[15] E. A. Winograd, R. Chitra, and M. J. Rozenberg. Orbital-selective crossover and Mott transitions in an asymmetric Hubbard model of cold atoms in optical lattices. *Phys. Rev. B*, 84:233102, Dec 2011.

[16] Sung-Sik Lee. Recent Developments in Non-Fermi Liquid Theory. *Annual Review of Condensed Matter Physics*, 9(1):227–244, 2018.

[17] E. A. Winograd, R. Chitra, and M. J. Rozenberg. Phase diagram of the asymmetric hubbard model and an entropic chromatographic method for cooling cold fermions in optical lattices. *Phys. Rev. B*, 86:195118, Nov 2012.

[18] J. K. Freericks and V. Zlatić. Exact dynamical mean-field theory of the Falicov-Kimball model. *Rev. Mod. Phys.*, 75:1333–1382, Oct 2003.

[19] Gábor Fáth, Zbigniew Domański, and Romuald Lemański. Asymmetric Hubbard chain at half-filling. *Phys. Rev. B*, 52:13910–13915, Nov 1995.

[20] Pavol Farkašovský. Phase diagram of the asymmetric Hubbard model. *Phys. Rev. B*, 77:085110, Feb 2008.

[21] M. Taglieber, A.-C. Voigt, T. Aoki, T. W. Hänsch, and K. Dieckmann. Quantum Degenerate Two-Species Fermi-Fermi Mixture Coexisting with a Bose-Einstein Condensate. *Phys. Rev. Lett.*, 100:010401, Jan 2008.

[22] Gregor Jotzu, Michael Messer, Frederik Görg, Daniel Greif, Rémi Desbuquois, and Tilman Esslinger. Creating State-Dependent Lattices for Ultracold Fermions by Magnetic Gradient Modulation. *Phys. Rev. Lett.*, 115:073002, Aug 2015.

[23] Ye-Hua Liu and Lei Wang. Quantum Monte-Carlo study of mass-imbalanced Hubbard models. *Phys. Rev. B*, 92:235129, Dec 2015.

[24] E. Fratini and S. Pilati. Zero-temperature equation of state and phase diagram of repulsive fermionic mixtures. *Phys. Rev. A*, 90:023605, Aug 2014.

[25] Dietrich Roscher, Jens Braun, Jiunn-Wei Chen, and Joaquín E Drut. Fermi gases with imaginary mass imbalance and the sign problem in Monte-Carlo calculations. *Journal of Physics G: Nuclear and Particle Physics*, 41(5):055110, mar 2014.

[26] Jens Braun, Joaquín E. Drut, and Dietrich Roscher. Zero-Temperature Equation of State of Mass-Imbalanced Resonant Fermi Gases. *Phys. Rev. Lett.*, 114:050404, Feb 2015.

[27] Alexandros Gezerlis, S. Gandolfi, K. E. Schmidt, and J. Carlson. Heavy-Light Fermion Mixtures at Unitarity. *Phys. Rev. Lett.*, 103:060403, Aug 2009.

[28] Peter Kroiss and Lode Pollet. Diagrammatic Monte-Carlo study of a mass-imbalanced Fermi-polaron system. *Phys. Rev. B*, 91:144507, Apr 2015.

[29] Marie-Therese Philipp, Markus Wallerberger, Patrik Gunacker, and Karsten Held. Mott-Hubbard transition in the mass-imbalanced Hubbard model. *The European Physical Journal B*, 90(6):114, Jun 2017.

[30] Tung-Lam Dao, Antoine Georges, and Massimo Capone. Competing superfluid and density-wave ground-states of fermionic mixtures with mass imbalance in optical lattices. *Phys. Rev. B*, 76:104517, Sep 2007.

[31] Tung-Lam Dao, Michel Ferrero, Pablo S. Cornaglia, and Massimo Capone. Mott transition of fermionic mixtures with mass imbalance in optical lattices. *Phys. Rev. A*, 85:013606, Jan 2012.

[32] Andrii Sotnikov, Daniel Cocks, and Walter Hofstetter. Advantages of Mass-Imbalanced Ultracold Fermionic Mixtures for Approaching Quantum Magnetism in Optical Lattices. *Phys. Rev. Lett.*, 109:065301, Aug 2012.

[33] A. B. Kuklov and B. V. Svistunov. Counterflow Superfluidity of Two-Species Ultracold Atoms in a Commensurate Optical Lattice. *Phys. Rev. Lett.*, 90:100401, Mar 2003.

[34] Ehud Altman, Walter Hofstetter, Eugene Demler, and Mikhail D Lukin. Phase diagram of two-component bosons on an optical lattice. *New Journal of Physics*, 5:113–113, sep 2003.

[35] A.L. Fetter and J.D. Walecka. *Quantum Theory of Many-Particle Systems*. McGraw-Hill, San Francisco, 1971.

[36] Ryan Levy, J.P.F. LeBlanc, and Emanuel Gull. Implementation of the maximum entropy method for analytic continuation. *Computer Physics Communications*, 215:149 – 155, 2017.

[37] Antoine Georges, Gabriel Kotliar, Werner Krauth, and Marcelo J. Rozenberg. Dynamical mean-field theory of strongly correlated fermion systems and the limit of infinite dimensions. *Rev. Mod. Phys.*, 68:13–125, Jan 1996.

[38] P. W. Anderson. Localized Magnetic States in Metals. *Phys. Rev.*, 124:41–53, Oct 1961.

[39] Walter Metzner and Dieter Vollhardt. Correlated Lattice Fermions in $d = \infty$ Dimensions. *Phys. Rev. Lett.*, 62:324–327, Jan 1989.

[40] Philipp Werner, Armin Comanac, Luca de' Medici, Matthias Troyer, and Andrew J. Millis. Continuous-Time Solver for Quantum Impurity Models. *Phys. Rev. Lett.*, 97:076405, Aug 2006.

[41] Emanuel Gull, Andrew J. Millis, Alexander I. Lichtenstein, Alexey N. Rubtsov, Matthias Troyer, and Philipp Werner. Continuous-time Monte-Carlo methods for quantum impurity models. *Rev. Mod. Phys.*, 83:349–404, May 2011.

[42] J. E. Hirsch and R. M. Fye. Monte-Carlo Method for Magnetic Impurities in Metals. *Phys. Rev. Lett.*, 56:2521–2524, Jun 1986.

[43] M. Jarrell. Hubbard model in infinite dimensions: A quantum Monte Carlo study. *Phys. Rev. Lett.*, 69:168–171, Jul 1992.

[44] Michel Caffarel and Werner Krauth. Exact diagonalization approach to correlated fermions in infinite dimensions: Mott transition and superconductivity. *Phys. Rev. Lett.*, 72:1545–1548, Mar 1994.

[45] Qimiao Si, M. J. Rozenberg, G. Kotliar, and A. E. Ruckenstein. Correlation induced insulator to metal transitions. *Phys. Rev. Lett.*, 72:2761–2764, Apr 1994.

[46] O. Sakai and Y. Kuramoto. Application of the numerical renormalization group method to the Hubbard model in infinite dimensions. *Solid State Communications*, 89(4):307 – 311, 1994.

[47] Daniel V. Schroeder Michael E. Peskin. *An introduction to quantum field theory*. Addison-Wesley, USA, 1995.

[48] C. Itzykson and J.-M. Drouffe. *Statistical field theory*. Cambridge University Press, Cambridge, 1989.

[49] Dieter Vollhardt. Dynamical MeanField Theory of Electronic Correlations in Models and Materials. *AIP Conference Proceedings*, 1297(1):339–403, 2010.

[50] Jun Kondo. Resistance Minimum in Dilute Magnetic Alloys. *Progress of Theoretical Physics*, 32(1):37–49, 07 1964.

[51] M. H. Hettler, M. Mukherjee, M. Jarrell, and H. R. Krishnamurthy. Dynamical cluster approximation: Nonlocal dynamics of correlated electron systems. *Phys. Rev. B*, 61:12739–12756, May 2000.

[52] M. Jarrell, Th. Maier, C. Huscroft, and S. Moukouri. Quantum Monte-Carlo algorithm for nonlocal corrections to the dynamical mean-field approximation. *Phys. Rev. B*, 64:195130, Oct 2001.

[53] E. Müller-Hartmann. Correlated fermions on a lattice in high dimensions. *Zeitschrift für Physik B Condensed Matter*, 74(4):507–512, Dec 1989.

[54] Nikolai V. Prokof'ev and Boris V. Svistunov. Polaron Problem by Diagrammatic Quantum Monte-Carlo. *Phys. Rev. Lett.*, 81:2514–2517, Sep 1998.

[55] Nicholas Metropolis, Arianna W. Rosenbluth, Marshall N. Rosenbluth, Augusta H. Teller, and Edward Teller. Equation of State Calculations by Fast Computing Machines. *The Journal of Chemical Physics*, 21(6):1087–1092, 1953.

[56] W. K. Hastings. Monte-Carlo Sampling Methods Using Markov Chains and Their Applications. *Biometrika*, 57(1):97–109, 1970.

[57] E. Gull, P. Werner, O. Parcollet, and M. Troyer. Continuous-time auxiliary-field Monte-Carlo for quantum impurity models. *EPL (Europhysics Letters)*, 82(5):57003, may 2008.

[58] K. Mikelsons, A. Macridin, and M. Jarrell. Relationship between Hirsch-Fye and weak-coupling diagrammatic quantum Monte-Carlo methods. *Phys. Rev. E*, 79:057701, May 2009.

[59] S. M. A. Rombouts, K. Heyde, and N. Jachowicz. Quantum Monte-Carlo Method for Fermions, Free of Discretization Errors. *Phys. Rev. Lett.*, 82:4155–4159, May 1999.

[60] A. Gaenko, A.E. Antipov, G. Carcassi, T. Chen, X. Chen, Q. Dong, L. Gamper, J. Gukelberger, R. Igarashi, S. Iskakov, M. Knz, J.P.F. LeBlanc, R. Levy, P.N. Ma, J.E. Paki, H. Shinaoka, S. Todo, M. Troyer, and E. Gull. Updated core libraries of the ALPS project. *Computer Physics Communications*, 213:235 – 251, 2017.

[61] Markus Wallerberger, Sergei Iskakov, Alexander Gaenko, Joseph Kleinhenz, Igor Krivenko, Ryan Levy, Jia Li, Hiroshi Shinaoka, Synge Todo, Tianran Chen, Xi Chen,

James P. F. LeBlanc, Joseph E. Paki, Hanna Terletska, Matthias Troyer, and Emanuel Gull. Updated Core Libraries of the ALPS Project. *arXiv e-prints*, page arXiv:1811.08331, Nov 2018.

[62] Philipp Werner, Takashi Oka, and Andrew J. Millis. Diagrammatic Monte-Carlo simulation of nonequilibrium systems. *Phys. Rev. B*, 79:035320, Jan 2009.

[63] Hiroshi Shinaoka, Emanuel Gull, and Philipp Werner. Continuous-time hybridization expansion quantum impurity solver for multi-orbital systems with complex hybridizations. *Computer Physics Communications*, 215:128 – 136, 2017.

[64] Johannes Ferber, Kateryna Foyevtsova, Roser Valentí, and Harald O. Jeschke. LDA + DMFT study of the effects of correlation in LiFeAs. *Phys. Rev. B*, 85:094505, Mar 2012.

[65] Emanuel Gull, Olivier Parcollet, and Andrew J. Millis. Superconductivity and the Pseudogap in the Two-Dimensional Hubbard Model. *Phys. Rev. Lett.*, 110:216405, May 2013.

[66] M. Louis Néel. Propriétées magnétiques des ferrites; férrimagnétisme et antiferromagnétisme. *Annales de Physique*, 12:137–198, 1948.

[67] N. D. Mermin and H. Wagner. Absence of Ferromagnetism or Antiferromagnetism in One or Two-Dimensional Isotropic Heisenberg Models. *Phys. Rev. Lett.*, 17:1133–1136, Nov 1966.

[68] IV Šimkovic, Fedor, J. P. F. LeBlanc, Aaram J. Kim, Youjin Deng, N. V. Prokof'ev, B. V. Svistunov, and Evgeny Kozik. Extended crossover from Fermi liquid to

quasi-antiferromagnet in the half-filled 2D Hubbard model. *arXiv e-prints*, page arXiv:1812.11503, Dec 2018.

[69] G. Rohringer, A. Valli, and A. Toschi. Local electronic correlation at the two-particle level. *Phys. Rev. B*, 86:125114, Sep 2012.

Appendix A

Second Order Approximation as Impurity Solver

In this section, we aim to show the coding procedure of the second-order perturbation theory for the one band lattice model, which can be used to solve the quantum impurity. Since the self-energy is momentum-independent, we are working in the local approximation. In the case where self-energy is purely local, the DMFT allows one to compute such local self-energy and local Green's function exactly by solving an auxiliary (quantum impurity) problem.

Let us start with the simplest one band Hubbard model:

$$H = \sum_k \varepsilon_k \hat{c}^\dagger_{k\sigma} \hat{c}_{k\sigma} + U \sum_i \hat{n}_{i\uparrow} \hat{n}_{i\downarrow} \tag{A.1}$$

Here, U is the onsite Coulomb interaction, and $\hat{c}^\dagger_{k\sigma}(\hat{c}_{k\sigma})$ creates (annihilates) an electron with spin σ and momentum k: $\hat{n}_{i\sigma} = \hat{c}^\dagger_{i\sigma}\hat{c}_{i\sigma}$. Dispersion energy ε_k is:

$$\varepsilon_k = -2t[cos(k_x) + cos(k_y)] \tag{A.2}$$

where t denotes the hopping amplitude between nearest neighbors.

The second order term of the self-energy, as Feynman diagram shows in Fig. A.1, is [69]:

$$\Sigma(\nu,k) = \frac{-U^2}{\beta^2} \sum_{\nu',\omega} \sum_{k,k',k''} G(\nu',k) G(\nu'+\omega, k'+k'') G(\nu+\omega, k'+k'') \tag{A.3}$$

where ν is external fermionic Mastubara frequency, ν' is also fermionic and ω is bosonic

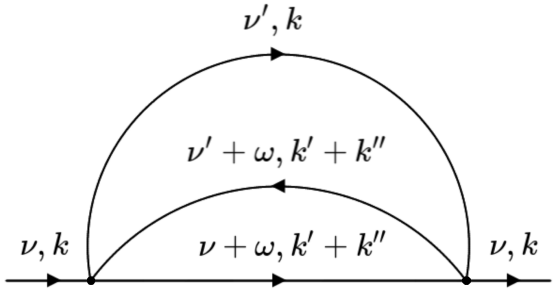

Figure A.1 – Feynman diagram of second order term of the self energy.

Mastubara frequency ($\nu = i\nu$, $\nu' = i\nu'$, $\omega = i\omega$). Since we are using the local approximation, the self-energy is momentum independent, i.e., $\Sigma(\nu,k) \approx \Sigma_{loc}(\nu)$. In order to have purely local self-energy, we need to replace the momentum dependent G_k in the Feynman diagram with the purely local counterpart G_{loc}. We will show later that the local Green's function is computed by an appropriate impurity problem. If we can solve the impurity problem exactly, we have the exact local Green's function.

The first step is evaluating a non-interaction Green's function which is defined as:

$$G^0(k,\nu_n) = \frac{1}{\nu_n - \varepsilon_k} \tag{A.4}$$

By using the Fourier transform at $r \equiv 0$ we get the local non-interacting Green's function:

$$G^0_{loc}(\nu_n) = \frac{1}{N_k} \sum_k \frac{1}{\nu_n - \varepsilon_k} \tag{A.5}$$

where $N_k = 1/2\pi^2$ is the normalization factor and ε_k is obtained by using Eq. (A.2). Thus, in the same way we can calculate three non-interacting local Green's function $G^0_{loc}(\nu')$, $G^0_{loc}(\nu' + \omega)$, and $G^0_{loc}(\nu + \omega)$, which leads to local self energy at specific U and β:

$$\Sigma(\nu) = \frac{-U^2}{\beta^2} \sum_{\nu',\omega} G^0_{loc}(\nu') G^0_{loc}(\nu' + \omega) G^0_{loc}(\nu + \omega) \tag{A.6}$$

Note that for finding $\nu'_n = (2n+1)\pi/\beta$ and $\omega_n = (2n)\pi/\beta$, we defined a cut off values which can be any finite values (should be big enough to have a precise value).

Next, the full Green's function is defined as:

$$G(k, \nu_n) = \frac{1}{\nu_n - \varepsilon_k - \Sigma(\nu_n)} \tag{A.7}$$

again using the Fourier transform at $r \equiv 0$, the impurity Green's function is:

$$G_{imp}(\nu_n) = \frac{1}{N_k} \sum_k \frac{1}{\nu_n - \varepsilon_k - \Sigma(\nu_n)} \tag{A.8}$$

which gives the new self energy:

$$\Sigma(\nu) = \frac{-U^2}{\beta^2} \sum_{\nu',\omega} G_{imp}(\nu') G_{imp}(\nu' + \omega) G_{imp}(\nu + \omega) \tag{A.9}$$

As Fig. 2.2 shows in the DMFT loop, we repeat the procedure until self-consistency is achieved, which in the final solution, $G_{imp} = G_{loc}$.

A.1 Results

In this section, we plot the local Green's function obtained by second-order approximation and compare them by the Green's function obtained by CT-AUX. It was shown that at

high temperature ($\beta = 1$) and low interaction (U=1), both methods are in good agreement with each other. However, by increasing the interaction (U=4), they differ, specially when $i\omega_n \to 0$ in their Green's function (see Fig. A.2).

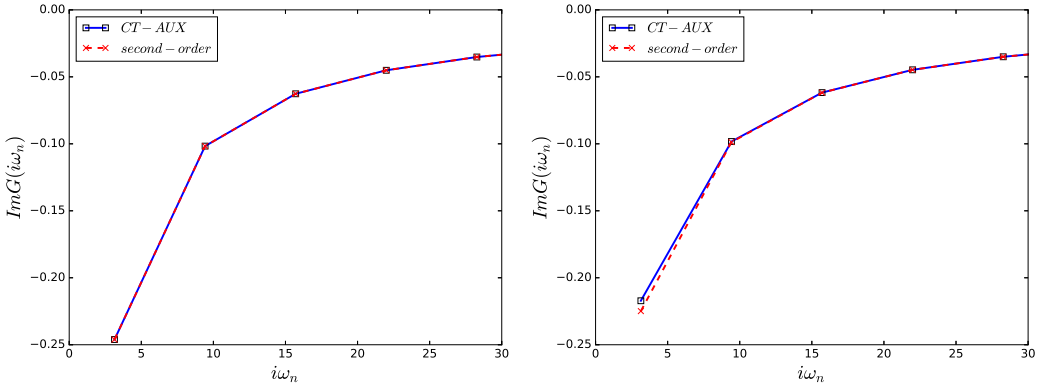

Figure A.2 – Green's function obtained by second-order and CT-AUX methods at $\beta = 1$ for HM when $t_f = 1$. *left*: U=0.5 and *right*: U=4

Appendix B

Figures to Obtain FL-nFL Crossover

In this section we illustrate how crossover diagrams Fig. 3.10 and Fig. 3.11 was obtained. We include all $\Delta\Sigma$ figures as a function of interaction U (Fig. B.1, Fig. B.2), mass-imbalance t_f (Fig. B.3, Fig. B.4) and inverse temperature β (Fig. B.5, Fig. B.6) which give us the crossover interaction U^*, mass-imbalance t_f^* and inverse temperature β^*. As described in Sec. 3.3, these figures show the variation of of $\mathrm{Im}\Sigma(i\omega_0)$ and $\mathrm{Im}\Sigma(i\omega_1)$ with U, t_f and β (ReΣ=0 at the Fermi surface).

Fig. B.1 and Fig. B.2 show the $\Delta\Sigma$ as a function of interaction U at different mass-imbalance and inverse temperatures. As we see in Fig. B.1 at t_f=0 for spin-down at U=2.0 and $\beta = 5$, the values of ImΣ at ω_0 are higher that ω_1, ($\Delta\Sigma > 0$), which is typical for a FL. As U is increasing, $\Delta\Sigma$ shows a trend towards nFL behavior by changing its sign. We mark this point as the onset of the nFL behavior in the crossover diagram Fig. 3.10. For spin-up at $t_f = 0$, we are in the nFL regime at any inverse temperature β and interaction strength U. Fig. B.3 and Fig. B.4 follow the same trends which give us crossover mass-imbalance at different interaction and inverse temperature. As mass-imbalance grows (t_f decreases),

there is a FL to nFL crossover. The crossover points obtained with these figures are used in both crossover diagrams Fig. 3.10 and Fig. 3.11. Finally, Fig. B.5 and Fig. B.6 show the $\Delta\Sigma$ as a function of inverse temperature at different mass-imbalance and interaction through which the crossover inverse temperatures are obtained. Here also we see that as temperature increases, there is a FL to nFL crossover. As we see in Fig. B.5 and Fig. B.6, $\Delta\Sigma_{\uparrow}$ at t_f=0 and any interaction and temperature is in nFL regime; however, for spin-down, there is a FL-nFL crossover at t_f=0. Let us here mention that since at U=3.5 and U=4 and t_f=0 we enter the AFM state, we are missing the t_f=0 curve. The crossover points obtained are used in crossover diagram Fig. 3.11.

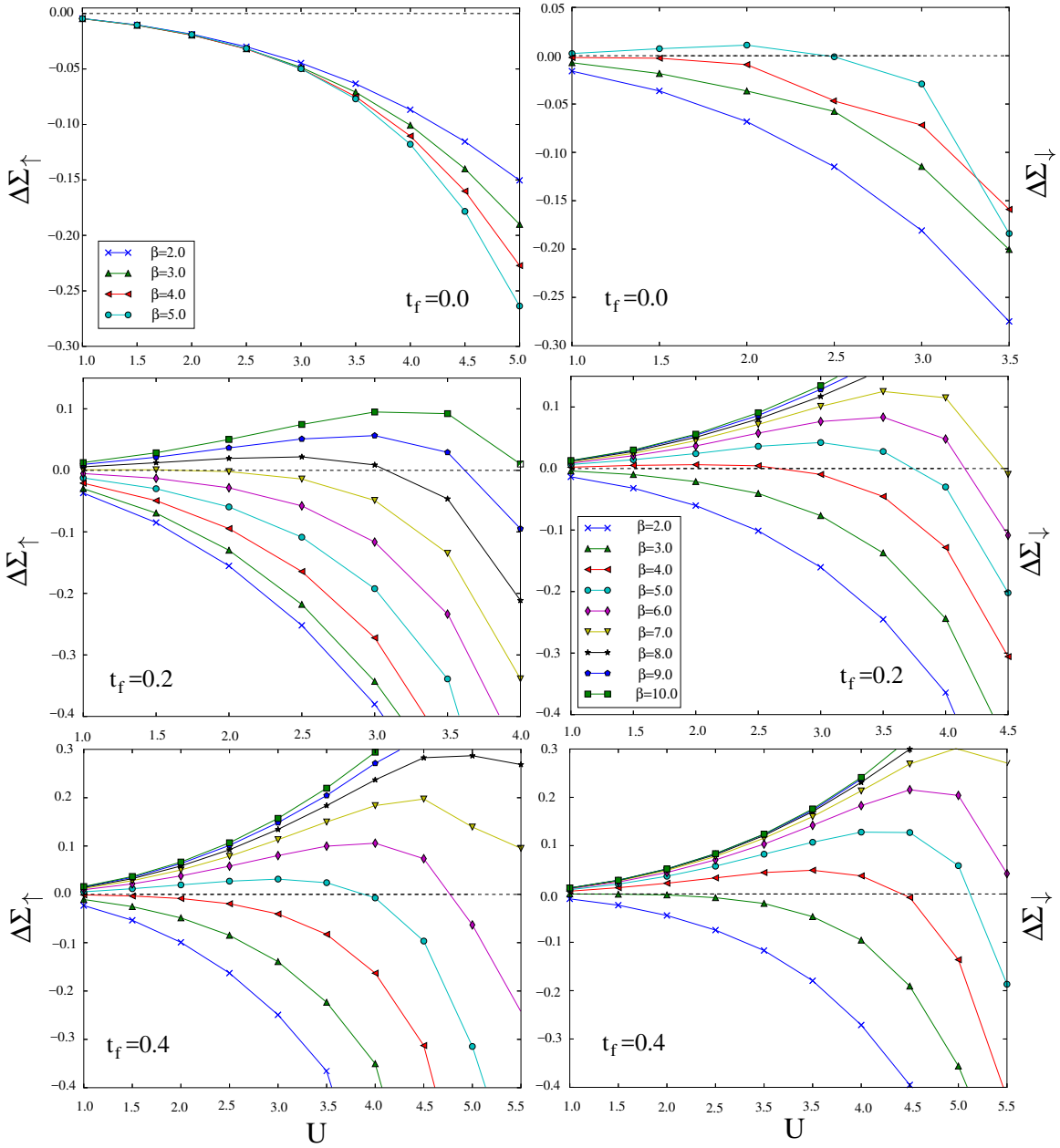

Figure B.1 – DMFT results for $\Delta\Sigma$ as a function of interaction at different inverse temperatures and $t_f = 0.0, 0.2, 0.4$.

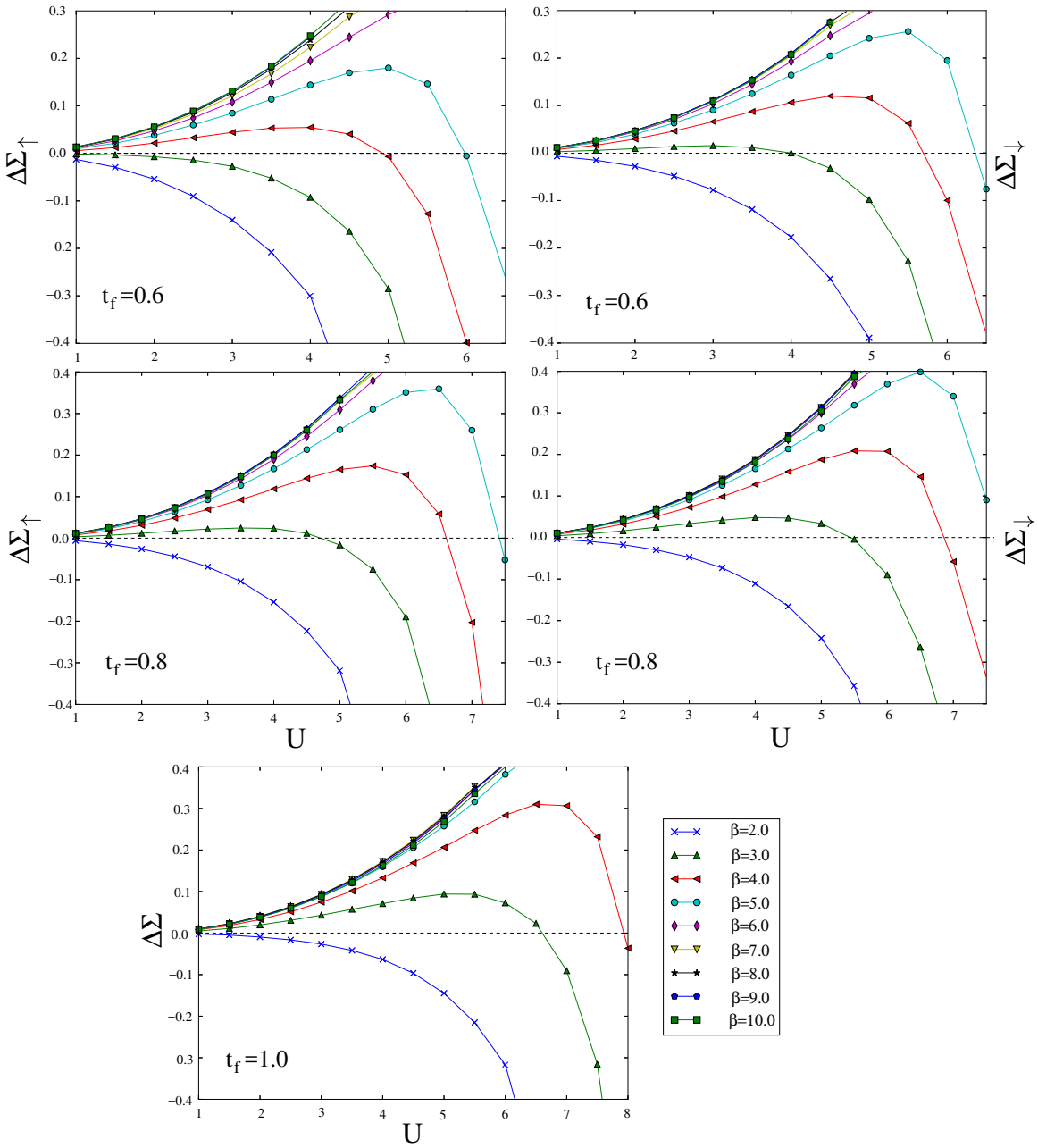

Figure B.2 – DMFT results for $\Delta\Sigma$ as a function of interaction at different inverse temperatures and $t_f = 0.6, 0.8, 1.0$.

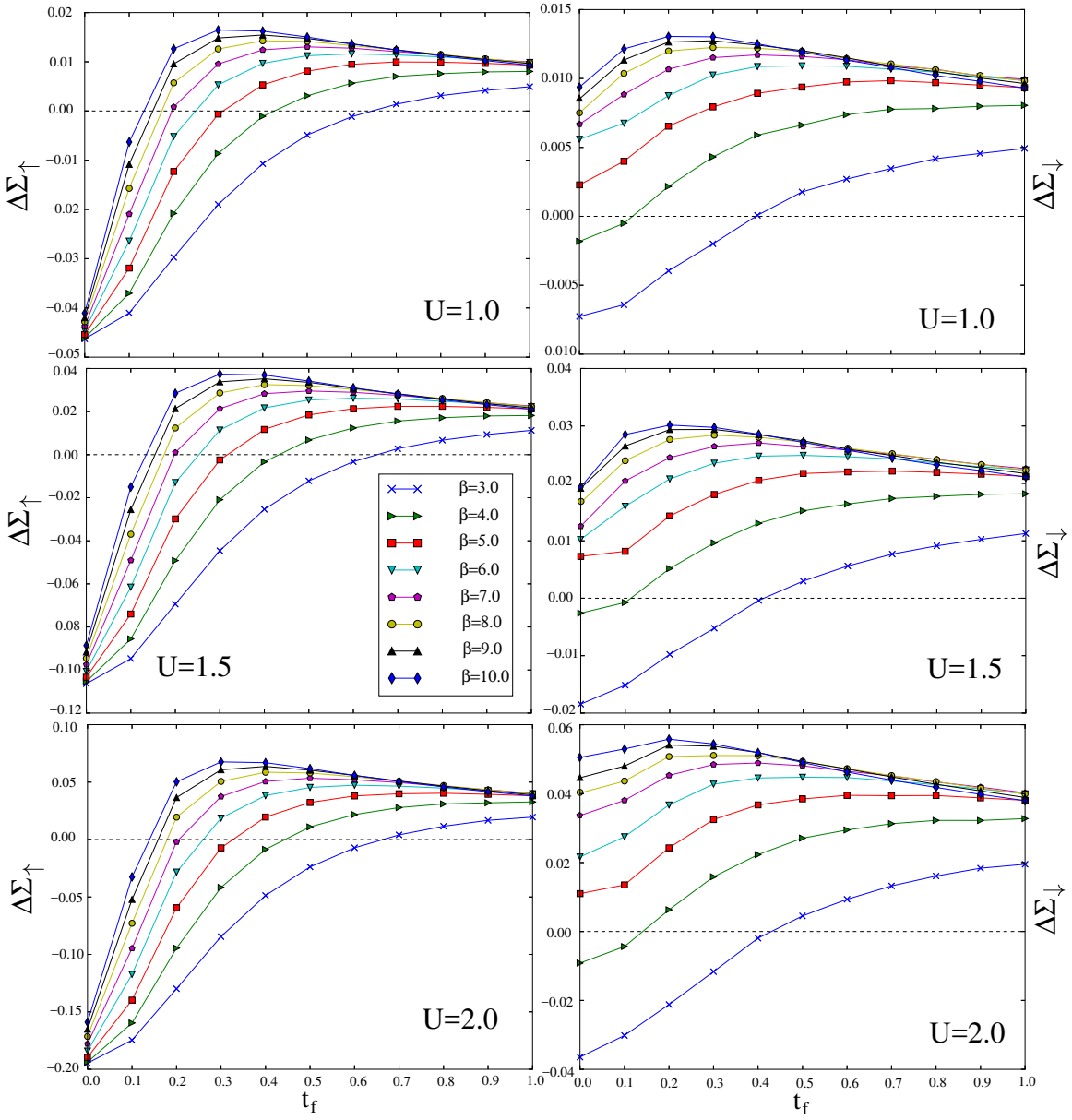

Figure B.3 – DMFT results for $\Delta\Sigma$ as a function of mass-imbalance at different inverse temperatures and $U = 1.0, 1.5, 2.0$.

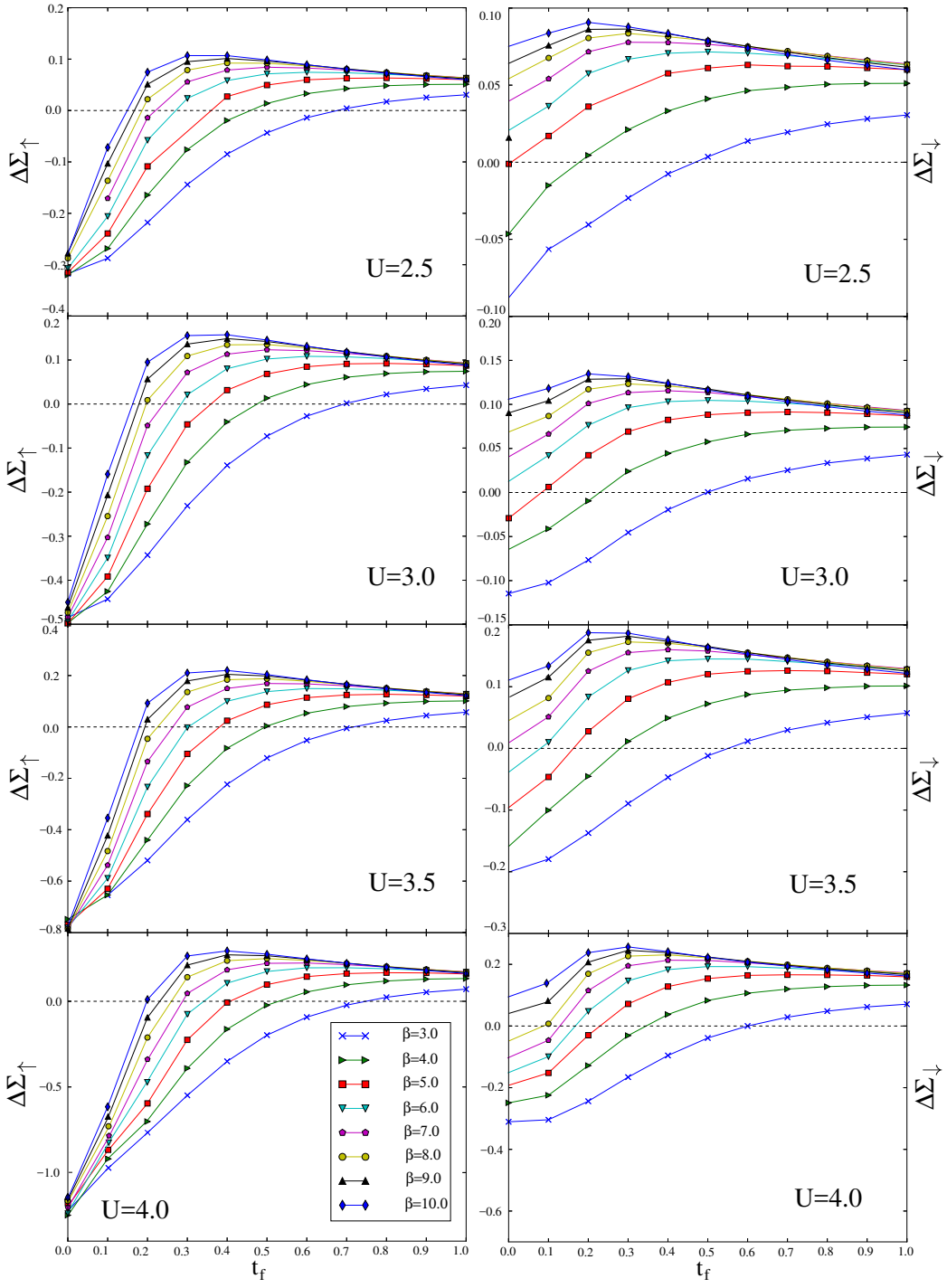

Figure B.4 – DMFT results for $\Delta\Sigma$ as a function of mass-imbalance at different inverse temperatures and $U = 2.5, 3.0, 3.5, 4.0$.

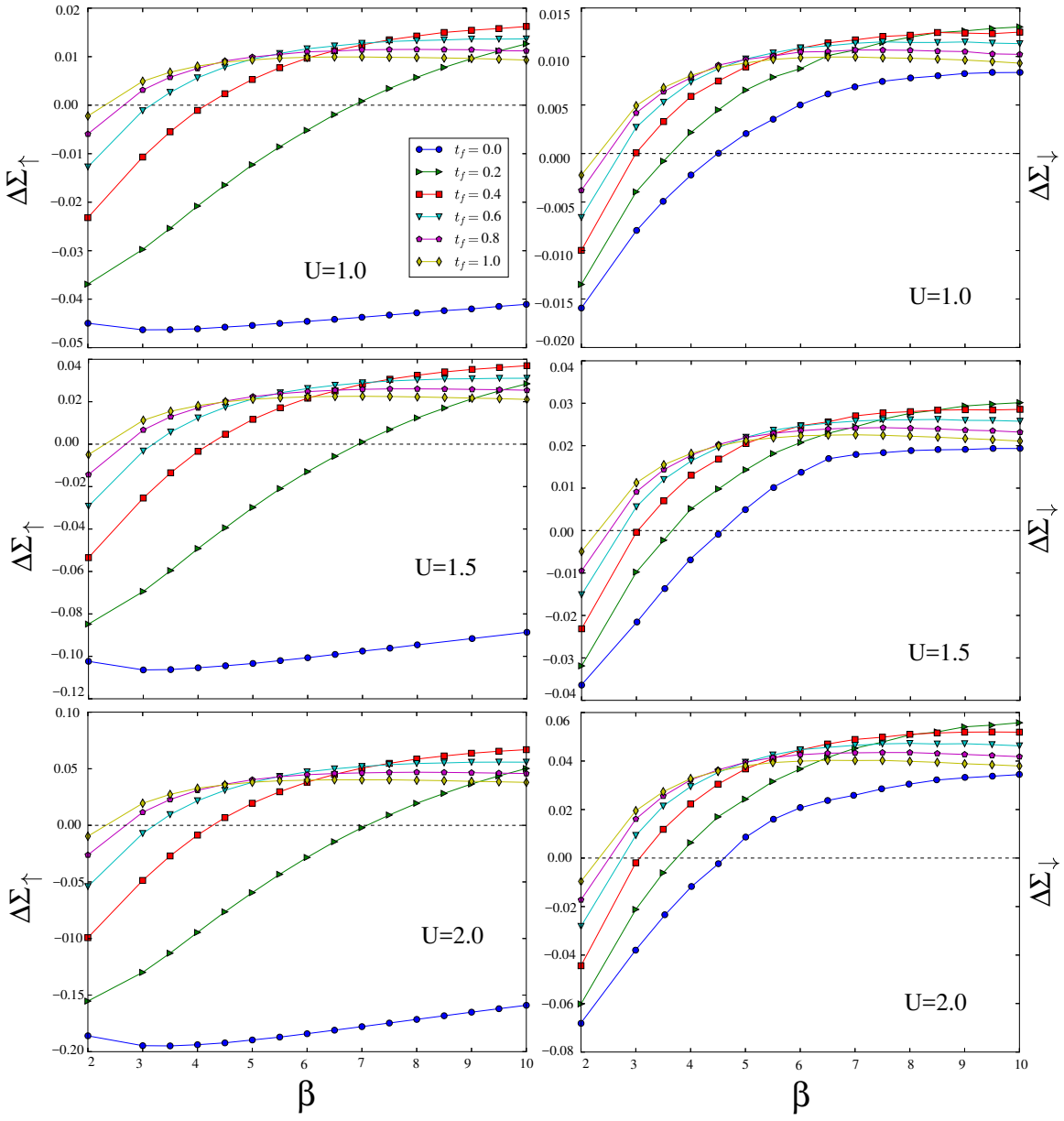

Figure B.5 – DMFT results for $\Delta\Sigma$ as a function of inverse temperatures at different mass-imbalance and $U = 1.0, 1.5, 2.0$.

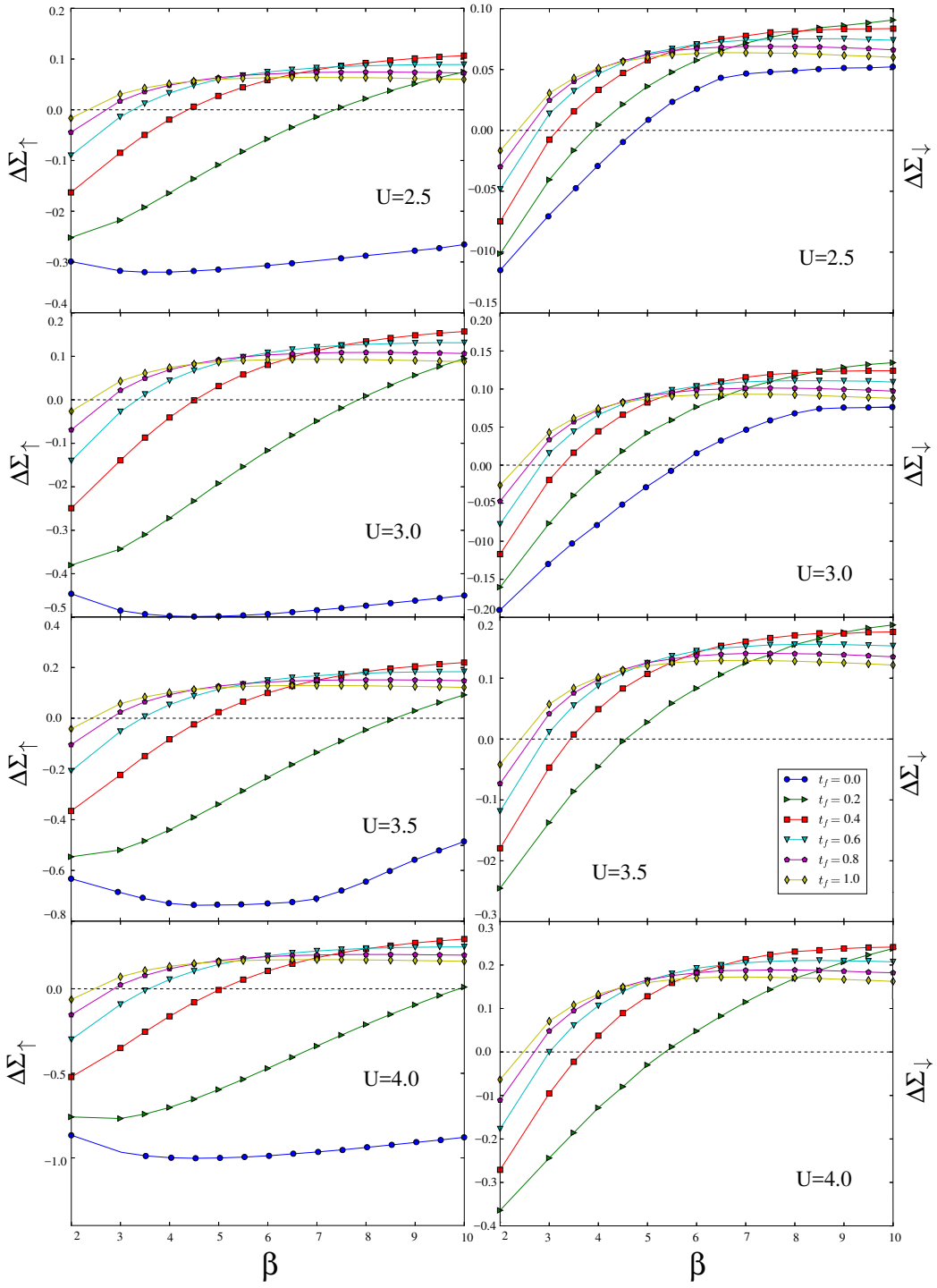

Figure B.6 – DMFT results for $\Delta\Sigma$ as a function of inverse temperatures at different mass-imbalance and $U = 2.5, 3.0, 3.5, 4.0$.